Title

Structural and Functional Ultra-short Echo Time (UTE) Proton Lung MRI: Techniques and Clinical Applications

Permalink

Author

Tan, Fei

Publication Date

2023

Peer reviewed|Thesis/dissertation

Structural and Functional Ultra-short Echo Time (UTE) Proton Lung MRI: Techniques and Clinical Applications

by

Fei Tan

DISSERTATION
Submitted in partial satisfaction of the requirements for degree of

DOCTOR OF PHILOSOPHY

in

Bioengineering

in the

GRADUATE DIVISION

of the

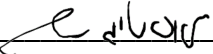UNIVERSITY OF CALIFORNIA, SAN FRANCISCO
AND
UNIVERSITY OF CALIFORNIA, BERKELEY

Approved:

DocuSigned by:

_____   Peder Larson
1644A2CD853841E...   Chair

DocuSigned by:

Marilynn Chan_____   Marilynn Chan
DocuSigned by:4F4...

_____   Michael Lustig
F5CC9412B1B242A...

_____

_____
                                                                                     Committee Members

Copyright 2023

by

Fei Tan

Acknowledgements

Contributions

Manuscripts submitted:

1. Pulmonary Ventilation Analysis Using 1H Ultra-Short Echo Time (UTE) Lung MRI: A Reproducibility Study. Fei Tan, Xucheng Zhu, Marilynn Chan, Nikhil Deveshwar, Matthew M. Willmering, Michael Lustig, Peder E. Z. Larson

2. Motion-Compensated Low-Rank Reconstruction (MoCoLoR) for Simultaneous Structural and Functional Ultrashort Echo Time (UTE) Lung MRI. Fei Tan*, Xucheng Zhu*, Marilynn Chan, Matthew A. Zapala, Shreyas S. Vasanawala, Frank Ong, Michael Lustig, Peder E. Z. Larson

3. 3D Free-Breathing Ultrashort Echo Time (UTE) 1H Ventilation Compared with Hyperpolarized 129Xe Ventilation and Pulmonary Function Testing, Fei Tan, Rachel L. Eddy, Vanessa M. Diamond, Jonathan H. Rayment, Peder E. Z. Larson

Abstract

Structural and Functional Ultra-short Echo Time (UTE) Proton Lung

MRI: Techniques and Clinical Applications

Fei Tan

UTE proton MRI is getting more attention in structural and functional lung imaging [1]. It improves signal-to-noise ratio (SNR) from low T2* tissues such as the lung parenchyma [2], and is motion robust compared to traditional Cartesian acquisitions. For radial UTE scans, the repeated acquisition of the center of k-space can serve as a self-navigator respiratory motion during free-breathing, enabling the motion-resolved 3D reconstruction at multiple respiratory states [3,4]. The volume change can then be assessed by the lung tissue deformation and intensity variation across the different respiratory phases, which is a straightforward biomarker for ventilation quantification. Compared to existing ventilation quantification methods such as pulmonary function testing (PFT), computed tomography (CT), and hyperpolarized noble gas MRI, 1H MRI offers local functionality via ventilation analysis, is non-ionizing, and does not require special equipment.

This dissertation aims to exploit the simultaneous structural and functional aspects of UTE 1H MRI. The first project explored ventilation quantification with free-breathing motion-resolved 3D UTE 1H lung MRI through the tissue deformation-based Jacobian determinant method. In the second project, we advanced on the motion-compensated low-rank constrained reconstruction, which jointly improves the motion field estimation and the reconstruction to get high-quality

ventilation maps and structural images. Third, we compared the 3D UTE 1H ventilation calculated from motion-compensated low-rank constrained reconstruction (MoCoLoR) [5,6] with the HP 129Xe ventilation for validation.

In addition, we investigated the feasibility of using a convolutional neural network for motion-compensated proton lung MRI reconstruction. It substantially accelerates the reconstruction for 3D radial UTE data, shortening the required reconstruction time from hours to minutes. It showed the potential to shorten the scan time, thus facilitating the clinical application of proton pulmonary UTE MRI. Moreover, we evaluated the imaging quality of UTE lung MRI in the pediatric population through a reader study. Lastly, we pushed the structural-functional proton 3D UTE lung MRI to clinical applications and reported results for pediatric patients with pectus deformity.

Table of Contents

List of Figures

List of Tables

Chapter 1 Introduction

1.1 Overview

Proton magnetic resonance imaging (MRI) has not yet been widely applied in clinical thoracic imaging because a) The lung has significantly lower proton density compared to other organs [7,8], b) the susceptibility induced by parenchyma-airway interface results in a short T2* [9], both of which contribute to a low signal, and c) the respiratory motion creates additional challenges to the acquisition.

Ultra-short echo time (UTE) MRI sequence [10] was introduced in 1991 for lung imaging. The half pulse and acquisition from the center enable an echo time as short as 50 microseconds. The ultra-short echo time compensates for the short T2* and enables higher signals in lung MRI. Motion-resolved 3D free-breathing pulmonary MRI techniques can utilize the motion and reconstruct image volumes at different respiratory states [4], minimizing motion artifacts and enabling functional analysis. This work aims to improve structural and functional UTE proton MRI techniques for clinical applications, especially for the pediatric population.

1.1.1 Clinical Lung Evaluation Approaches

Pulmonary function testing remains the primary clinical routine for lung disease evaluation [11], but it only provides global ventilation. The dependence on patient effort also limits its use in young children and infants [12].

Computed tomography is preferred when a chest X-ray is not sufficient [13]. It provides fast acquisition and high-resolution structure information of the lung. However, the ionizing radiation from CT can be harmful to children.

Hyperpolarized noble gas MRI such as 3He or 129Xe acquires static and dynamic images of airways within a single breath-hold with the noble gases [14]. However, HP gas MRI requires specialized equipment, including a polarizer, and unique RF coils, so it can only be performed at a few sites worldwide.

1.1.2 Existing Proton MRI Studies

Previous studies on free-breathing proton MRI for lung function evaluation exist. Fourier decomposition [15] acquires consecutive 2D MRIs, applies Fourier decomposition along the time dimension at each pixel, and then separates cardiac and pulmonary motion by frequency spectrum. The total area-under-curve at typical frequencies for the respiratory and cardiac cycle provides the ventilation and perfusion maps, respectively.

Phase-resolved functional lung imaging (PREFUL) [16] built on the concept of Fourier decomposition. It reorders the images according to the cardiac or respiratory motion phase and reconstructs one complete cardiac/respiratory cycle. This method sheds light on perfusion and ventilation map calculation by proton MRI. The caveat of this approach is that it only deals with 2D images, and the registration can be unreliable.

The recent effort also includes flow-volume loop [17] quantification. The local fractional ventilation and its derivation against time at each time point form a flow-volume loop. The flow-volume loop of an abnormal lung deviates from that of the healthy cohort.

Structural lung MRI has also seen significant developments in the past decade. While respiratory motion remains problematic for conventional reconstruction methods, the recently developed motion-resolved 3D free-breathing pulmonary instead MRI utilizes the motion. It groups the acquired k-space signal by the motion state and then reconstructs image volumes at different respiratory states [4].

For example, XD-GRASP [18] applies the total variation (TV) constraint along the motion states dimension and demonstrated application in pulmonary and cardiac MR. Other methods for motion compensation have been introduced and demonstrated for lung MRI, such as iMoCo [19] and MostMoCo [20]. The motion fields are included in the data consistency term for an improved motion-resolved reconstruction in these methods.

1.1.3   Aim

This dissertation aims to improve the ventilation quantification and image reconstruction of free-breathing motion-resolved 3D UTE 1H lung MRI, especially for pediatric applications.

1.2   Outline

Chapter 2 summarizes MR basics related to UTE 1H Lung MRI.

Chapters 3-5 discuss developed approaches. Chapter 3 introduces a functional analysis method, pulmonary ventilation analysis using 1H ultra-short echo time UTE lung MRI: a reproducibility study. Chapter 4 discusses a reconstruction approach for UTE lung MRI: motion-compensated low-rank constrained reconstruction (MoCoLoR) for simultaneous structural and functional ultrashort echo time (UTE) lung MRI. Chapter 5 presents validation of 1H ventilation using a multi-nuclear MRI approach, titled 3D Free-Breathing ultrashort echo time (UTE) 1H ventilation compared with hyperpolarized 129Xe ventilation.

Chapters 6-8 present exploratory results and applications. Chapter 6 summarizes a machine learning-based project, iterative motion-compensated reconstruction with convolutional neural network (iMoCo-Net) for ultrashort echo time (UTE) proton lung MRI. Chapter 7 covers a reader study, quality assessment of ultrashort echo time proton lung MRI in pediatric patients. Chapter 8 presents a clinical application study, structural and functional proton UTE lung MRI in pediatric pectus deformity patients.

Lastly, Chapter 9 summarizes the work and discusses future directions for UTE lung MRI research.

Chapter 2 MR Basics and Reconstruction

2.1 MR Basics

2.1.1 Overview (B0, B1, Gradients)

Three key components enabled Magnetic Resonance Imaging (MRI). First, an external static magnetic field B0 will align the nuclear spins with the field direction. By convention, this direction is defined as the longitudinal direction. In addition, the nuclear spins will rotate at a well-defined frequency called Larmor frequency. Second, a radiofrequency (RF) pulse resonating at the Larmor frequency B1 will disturb the equilibrium and tip the spins to the transverse plane. The receiver coils can then detect the electromotive force (EMF) signal. Third, linear gradient fields Gx, Gy, Gz along the transverse plane and the longitudinal axis (x, y, z coordinates) enable spatial localization of the signal [21]. Figure 2.1 illustrates an MRI scanner cutaway with the key components.
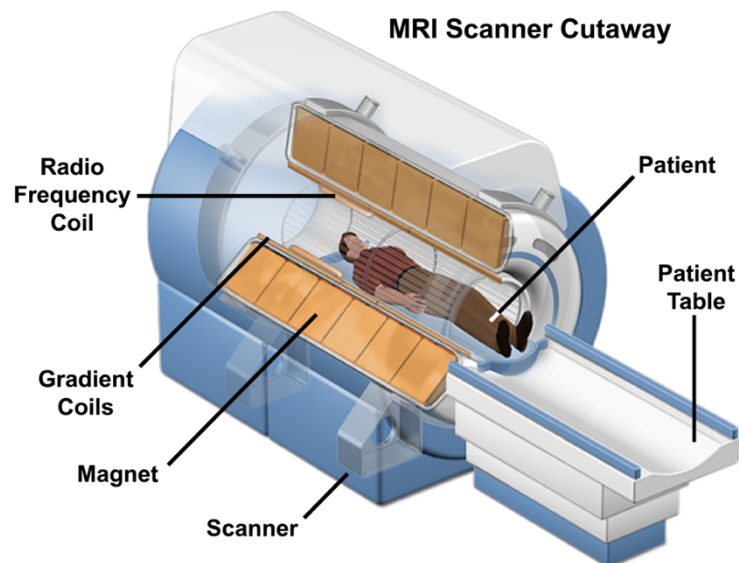
Figure 2.1 MRI Scanner Cutaway. [22]

2.1.2 Relaxation (T1, T2)

MRI distinguishes different types of tissues based on their intrinsic properties, such as the longitudinal relaxation time (T1) and transverse relaxation time (T2). Specifically, the longitudinal relaxation time describes the time it takes for nuclear spins to return to equilibrium and align with the main magnetic field after disturbance. The transverse relaxation time describes how the spins disperse, resulting in signal decay in the transverse plane [21].

2.1.3 Contrast (TR, TE)

Imaging sequence parameters TE (echo time) and TR (repetition time) accentuate the image contrast. TE is defined as the time between the center of the RF pulse and the time that the k-space center is measured, while TR refers to the time interval between two repetitively applied RF pulses [23].

2.2 Pulse Sequence

2.2.1 Ultrashort Echo Time (UTE) Sequence

Pulse sequences with a short echo time (TE) in the 50-200 millisecond range are usually categorized as ultrashort echo time sequences [24]. These sequences are suitable for imaging short $T2^*$ tissues such as the lung parenchyma ($T2^*$ 0.5-3 ms). The center of k-space is sampled first for each readout to achieve ultrashort echo time, resulting in a non-Cartesian trajectory. Figure 2.2 demonstrates a pulse sequence diagram for a basic 2D UTE sequence.
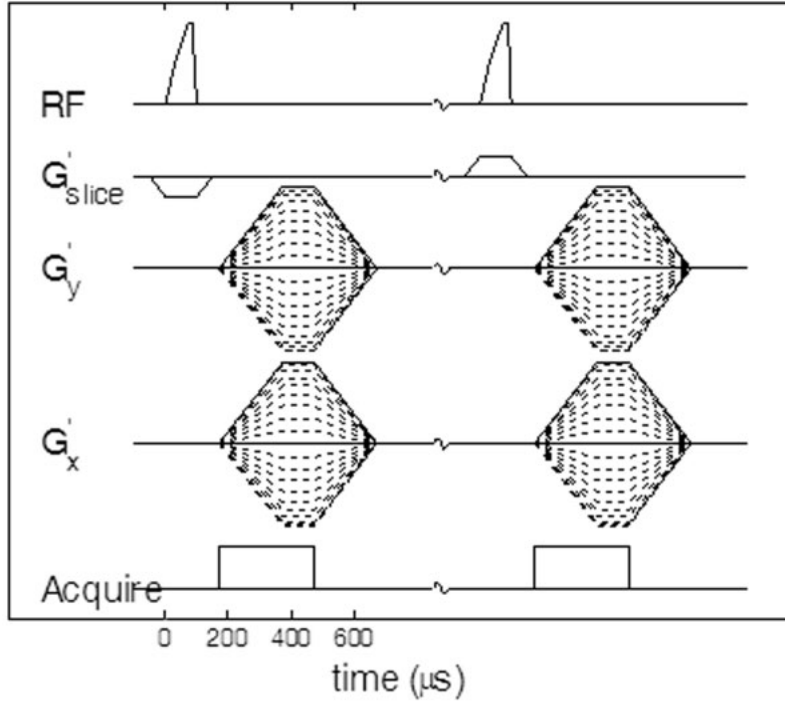
Figure 2.2 Pulse sequence diagram for a basic UTE sequence [25].

The conventional UTE is less efficient compared to the Cartesian approach. Signal-to-noise ratio (SNR) and image quality need to be improved to make UTE sequence clinically applicable. Our studies adopted an optimized 3D radial pulse sequence developed by Johnson et al. [26]. As shown in the pulse sequence diagram in Figure 2.3, the sequence consists of a slab selective half pulse followed by a center-out k-space acquisition. Instead of a constant gradient, the gradient strength is optimized as $g(s) < \min(\left|\frac{A}{s^2}\right|, G_{max})$. Where g represents the gradient strength, s is the position along the spokes, and A is an arbitrary scaling factor, G_{max} is the maximum gradient achievable by the scanner.
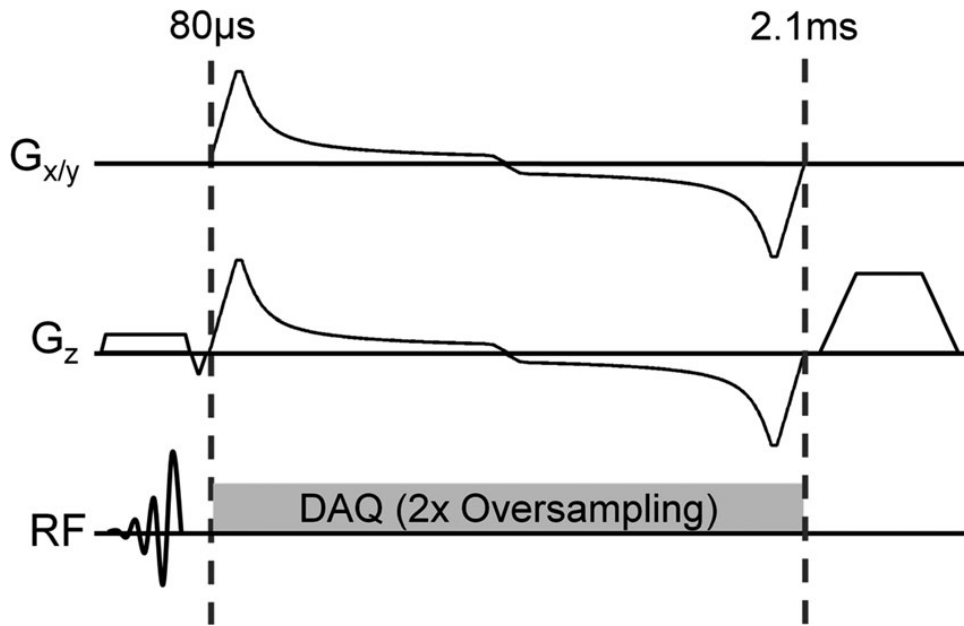
Figure 2.3 Pulse sequence diagram for efficiency-optimized variable density 3D UTE [26].

2.2.2   Golden Angle Ordering

Golden angle ordering is a pseudo-random ordering scheme for acquisition trajectories [27]. It has

the advantage of motion robustness, incoherent image artifacts, and is available for image sorting

and binning. The golden angle is derived from the golden ratio $(1 + \sqrt{5})/2 \approx 1.618$. For half

radial spokes, the rotation angle is defined as 137.51°, where each following spoke slices the

largest angle into two segments. The derivation of 2D radial golden angle is shown in Figure 2.4.

Figure 2.4 Golden ratio of line segment and golden angle of 2D radial spokes [27].

The pseudo-random property of golden angle ordering is well-suited for respiratory motion binning, as shown in Figure 2.5. Compared to sequential trajectory ordering, it provides more uniform k-space coverage after respiratory motion binning.
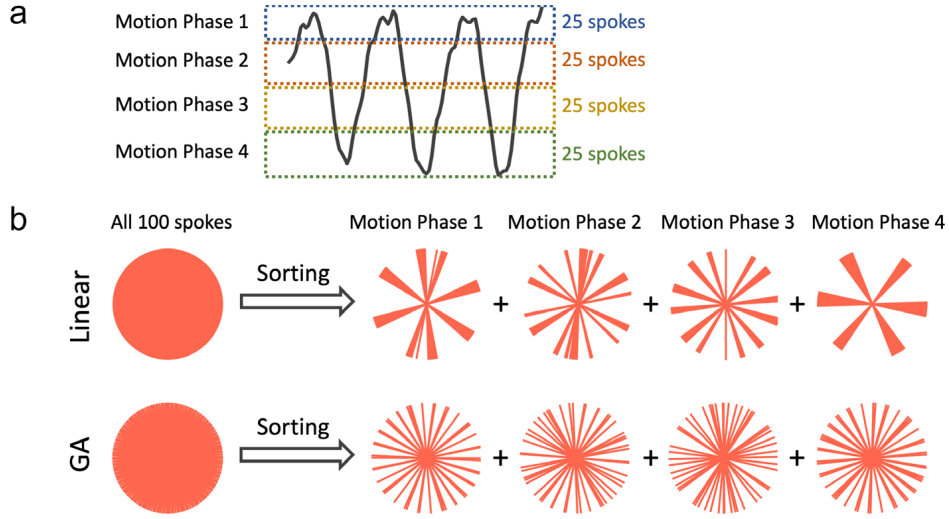
Figure 2.5 Golden angle ordering offers uniform k-space coverage after motion binning compared to sequential ordering [27].

2.3 Reconstruction

2.3.1 Iterative Reconstruction

A generalized reconstruction can be formulated as follows,

$$\underset{\hat{X}}{\mathrm{argmin}}\left\|E\hat{X} - d\right\|_2^2 + \lambda R(\hat{X})$$

Where $\hat{X}$ is the MR image to be restored, d is the data collected in k-space, E is a combination of linear operators that transforms the image to k-space, and R is a regularization term.

However, respiratory motion can cause significant blurring with conventional image reconstruction. Motion-compensated reconstruction, such as iterative motion-compensated reconstruction (iMoCo) [19], is developed to address this issue. The optimization problem is formulated as follows.

$$\underset{\hat{X}}{\mathrm{argmin}}\sum_{i,k}^{N,m}\left\|W\left(FSM\hat{X} - d_{ik}\right)\right\|_2^2 + \lambda_s TGV_s(\hat{X})$$

10

Where M represents the motion field, S is the sensitivity map, F is the nonuniform Fourier transform, W is the sampling density compensation factor, and TGV is the spatial total generalized variation sparsity constraint.

The iMoCo technique provided an essential foundation for the presented work by addressing the challenging respiratory motion in lung MRI. This technique involves binning the data according to respiratory states and applying an extra dimension reconstruction to compute motion-resolved images. Afterward, registrations are performed between each respiratory state and the end-expiratory state, and the resulting motion fields are incorporated into the iterative motion-compensated reconstruction optimization problem.

2.3.2 Respiratory Binning & Motion Field Estimation

Respiratory binning is crucial for motion-compensated reconstruction and ventilation analysis. Respiratory motion can be recorded by an external device or sampling the center of k-space. Subsequently, the raw data can be regrouped based on the amplitude or timing of the respiratory motion. Details on respiratory binning tailored for each project are discussed in the methods section of the following chapters.

Motion field estimation also plays a vital role in motion-compensated reconstruction. Chapter 3 compares two registration approaches that estimate the motion field and expand on its relationship with ventilation map calculation.

Chapter 3 Pulmonary Ventilation Analysis Using 1H Ultra-Short Echo Time (UTE) Lung MRI Evaluated with A Reproducibility Study

3.1 Introduction

[1]H MRI has recently been explored as a radiation-free alternative for lung ventilation evaluation [7,28]. The Fourier decomposition method [29] acquires consecutive 2D MRIs, applies Fourier decomposition along the time dimension at each pixel, and then separates the cardiac motion and pulmonary motion by the frequency spectrum. Phase-resolved functional lung imaging (PREFUL) [16] reorders the images according to the phase of the cardiac or respiratory motion and reconstructs one full cardiac/respiratory cycle. The flow-volume loop [30] regional ventilation is also introduced.

UTE MRI is favorable for free-breathing lung imaging [10,24] because it is robust to motion artifacts and improves signal-to-noise ratio (SNR) from low $T2^*$ tissues such as the lung parenchyma [2]. The center of k-space can serve as a self-navigator that tracks respiratory motion during data acquisition [4,18]. By grouping the k-space data acquired at different respiratory states, we can reconstruct lung images at these states with minimal motion artifacts, which are the basis of ventilation analysis. Examples include XD-GRASP [18] and self-navigated motion-resolved reconstruction [4].

In this work, we evaluated methods for lung ventilation quantification with a free-breathing respiratory phase-resolved 3D radial UTE lung MRI. We evaluated the effects of two registration

methods and two ventilation quantification methods by a reproducibility study in healthy

volunteers.

3.2 Methods

Study Design

All procedures were approved by the University of California, San Francisco's Institutional

Review Board (IRB). 6 healthy volunteers (age 23 - 30, 3 Female, 3 Male) were recruited to the

study and written consent was acquired before their scan. Eligibility criteria were no history of

asthma or smoking.

An efficiency and SNR optimized variable-density 3D radial UTE sequence [31] with golden angle

ordering was used on a 3T clinical scanner (Discovery MR750, GE Healthcare, Waukesha, WI)

with an 8-channel cardiac phased-array coil (GE Healthcare, Waukesha, WI). Volunteers

performed tidal breathing in a supine position. The key scan parameters were: flip angle=4°,

FOV=40cm isotropic, TE/TR=0.1/2.4ms, BW=±125kHz, readout points=512, spokes=200,000,

resolution=2.5mm isotropic (Figure 3.1 A). For studying reproducibility, we scanned each

subject with the same sequences twice in the same day, 30 minutes apart, re-setting up the coils

between the scans. The pipeline for the study is shown in Figure 3.1.

Image Processing

Reconstruction

The reconstruction was completed by MATLAB (Mathworks 2019a) and the BART (Berkeley

Advanced Reconstruction Toolbox) [32]. The data were first binned into 12 phases according to

their respiratory cycle timing (Figure 3.1 B, C, D) derived from the center of k-space [4]. The number of phases was chosen to balance between less streaking artifacts and more respiratory phases. The respiratory motion was extracted from the coil with the strongest signal fluctuation around the breathing frequency. A 4D phase-resolved image series with three spatial dimensions plus a respiratory phase dimension were reconstructed by parallel imaging and compressed sensing (PICS) reconstruction (Figure 3.1 E).

Registration

Then, we registered the image of each respiratory state to the end-expiration state (Figure 3.1 F) with two different methods: 1) B-spline 3D+t cyclic registration [33] to utilize the cyclic characteristic of breathing pattern, and 2) the 3D symmetric image normalization (SyN) method [34] with mutual information metric to minimize the effect of intensity change during breathing. The registrations were implemented in Elastix [35] and ANTs [36] toolboxes, respectively. Both methods utilized 4-level multiscale registration.

Segmentation

Segmentation of the left and right lung was achieved by a pre-trained U-Net deep learning algorithm from [37].

Ventilation Analysis

Regional Ventilation

Regional ventilation was calculated based on the local lung tissue motion and deformation information. The Jacobian determinant (JD) of the registration motion field (D) represents the

ratio of volume at each respiratory state, V_{resp}, to the end-expiration state, $V_{end-expi}$. JD >1

means expansion and JD<1 means contraction. The definition was as follows [38,39],

$$JD = \frac{V_{resp}}{V_{end-expi}} = \left| \det \left[\text{Id} + \frac{\partial (D_x, D_y, D_z)}{\partial (x, y, z)} \right] \right|$$

where x,y,z were the spatial dimensions and Id was a 3-by-3 identity matrix.

The regional ventilation definition from [40] was adopted to show the local percentage lung volume

change by subtracting 1:

$$Regional\ Ventilation = \frac{V_{resp} - V_{end-expi}}{V_{end-expi}} = JD - 1.$$

Specific Ventilation

Specific ventilation [41,42] was calculated by the percentage intensity difference at each respiratory

state to the end-expiration state, measured using the registered images. The definition was as

follows,

$$Specific\ Ventilation = \frac{V_{resp} - V_{end-expi}}{V_{end-expi}} = \frac{\frac{m}{\rho}_{resp} - \frac{m}{\rho}_{end-expi}}{\frac{m}{\rho}_{end-expi}} = \frac{S_{end-expi} - S_{resp}}{S_{resp}}$$

where $S_{end-expi}, S_{resp}$ were the signal intensities of each voxel in the end-expiratory and other

respiratory states, m was the total mass, and $\rho_{end-expi}, \rho_{resp}$ were the proton densities. This

metric assumes conservation of mass and $S \propto \rho$.

A Gaussian filter of matrix size 5x5x5 voxels was applied on the spatial domain and a 1D

wrapped Gaussian filter was applied in the phase dimension for noise reduction.

Statistical Analysis

Details of statistical analysis and image-based pulmonary function measurement are included in the supplementary material.

All scripts for this paper are available online at

https://github.com/PulmonaryMRI/reproducibility.
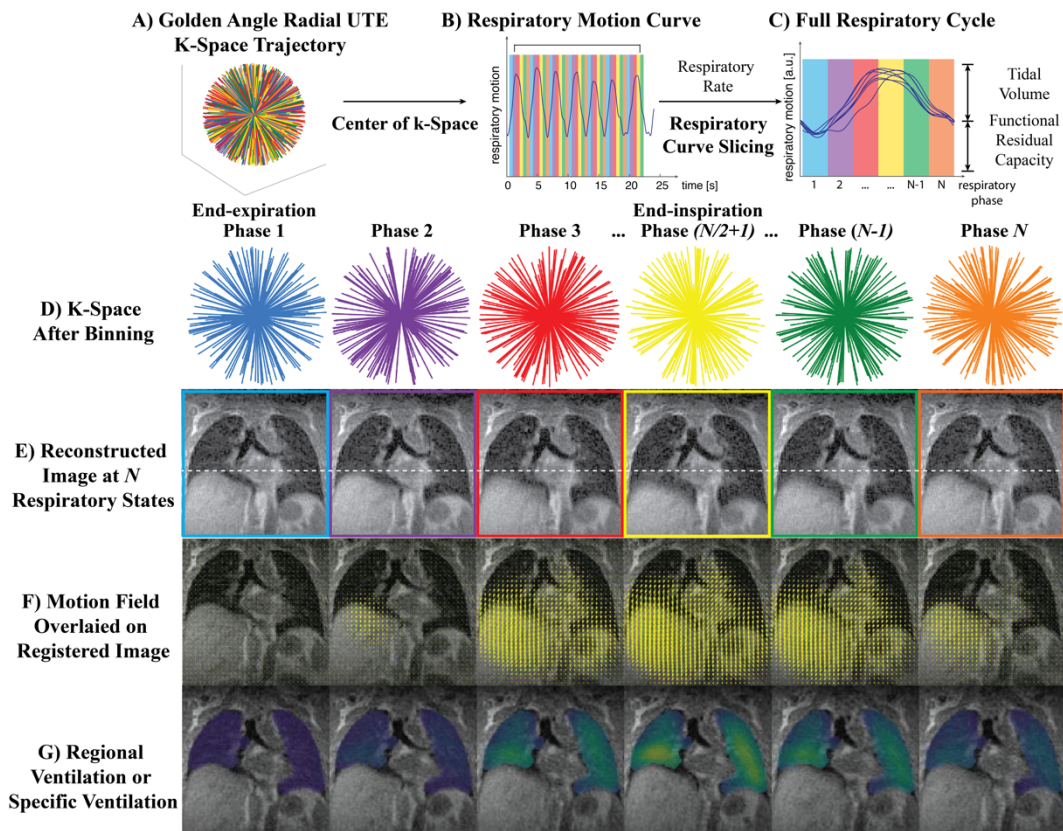
Figure 3.1 Pipeline for Ventilation Analysis of UTE Lung MRI with N Respiratory Phases.

Note that the same procedure is performed twice on the same day for reproducibility studies. A) Data acquisition. B-E) Image reconstruction, the color coding represents respiratory phases. F) Image registration, three types of image registration methods were experimented. G) Ventilation analysis, the Jacobian determinant of the motion field vector at each voxel minus 1, represents the regional ventilation percentage.

3.3 Results

Representative Ventilation Maps

Figure 3.2 depicts the ventilation map overlayed on the registered phase-resolved lung MR images for the two registration methods and two ventilation calculation methods of one representative volunteer.

The ventilation maps for phase 1 depict the cyclic consistency of the methods. Since phase 1 is the end-expiration state and is selected to be the reference frame, the ventilation of this frame should be close or equal to 0. The intensity-based methods guaranteed it. However, for Jacobian determinant-based methods, the concatenated motion fields may not be zero if cyclic consistency is not enforced. For regional ventilation, the B-spline cyclic registration is closer to zero at phase 1, indicating that it mimics the cyclic respiratory pattern.

The regional ventilation maps show a smoother pattern compared to specific ventilation. The smoothness of regional ventilation could result from the smoothing filter applied on the motion field during registration.
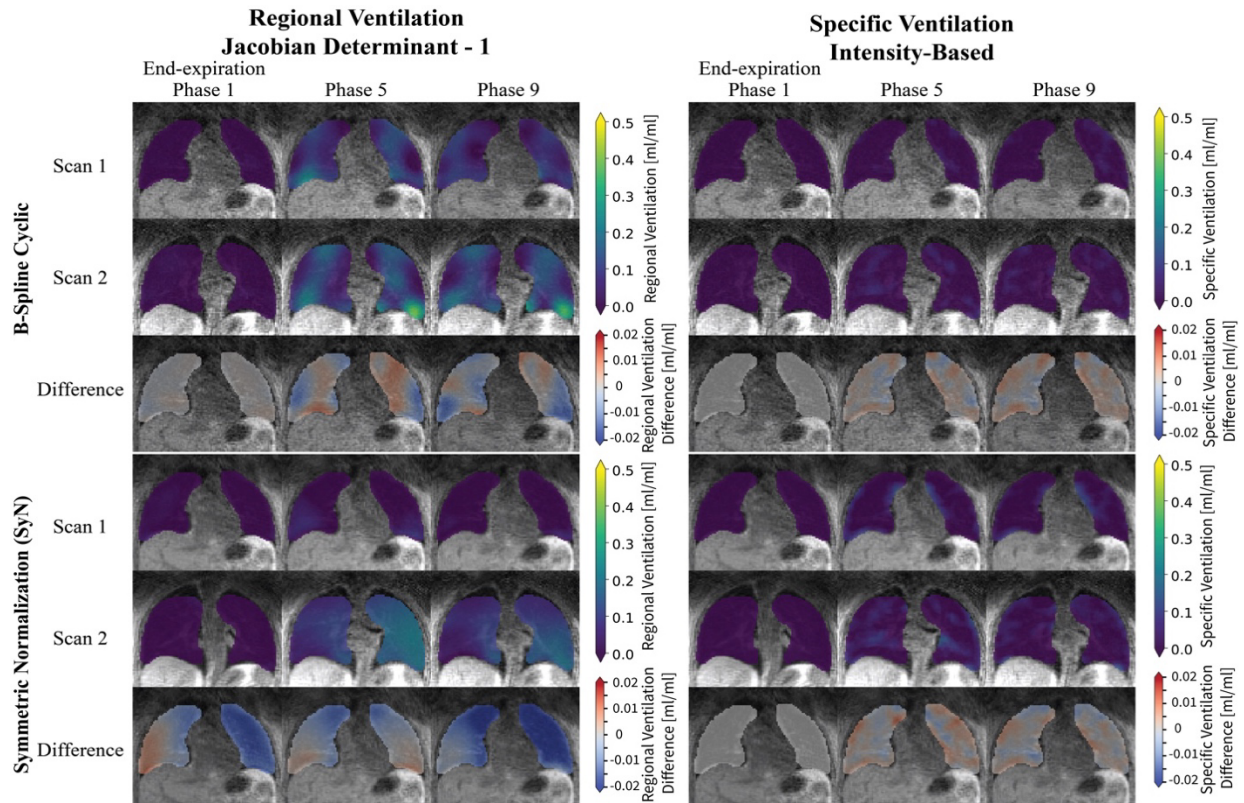
Figure 3.2 Representative Regional Ventilation Map of Two Scans and Their Difference Using Three Registration Methods.

Within each method, the first row and second row are from the first and second scan respectively while the third row is the difference of ventilation maps between the two after a simple registration. A regional ventilation of 0.1 correspond to 10% of volume expansion with respect to the end-expiration state. For conciseness, three respiratory phases out of twelve are shown.

Reproducibility

Intra-Subject Analysis

Figure 3.3 shows the ventilation distributions for two representative volunteers with two registration methods and two ventilation calculation methods. This includes consistent (Volunteer 6) and inconsistent (Volunteer 5) breathing between the two scans. In the split violin plots of all four combinations (columns 1-4), the median regional or specific ventilation evolves with a generally increase-decrease pattern, following the respiratory phases and matching the segmentation-based tidal volume measurements (column 5). We also computed the correlation

18

(column 6) between lung volume measurements based on these ventilation metrics and segmented volumes across respiratory phases. For all cases, the regional ventilation approach (blue and orange) has higher Pearson correlation coefficients, r, compared to the specific ventilation approach.
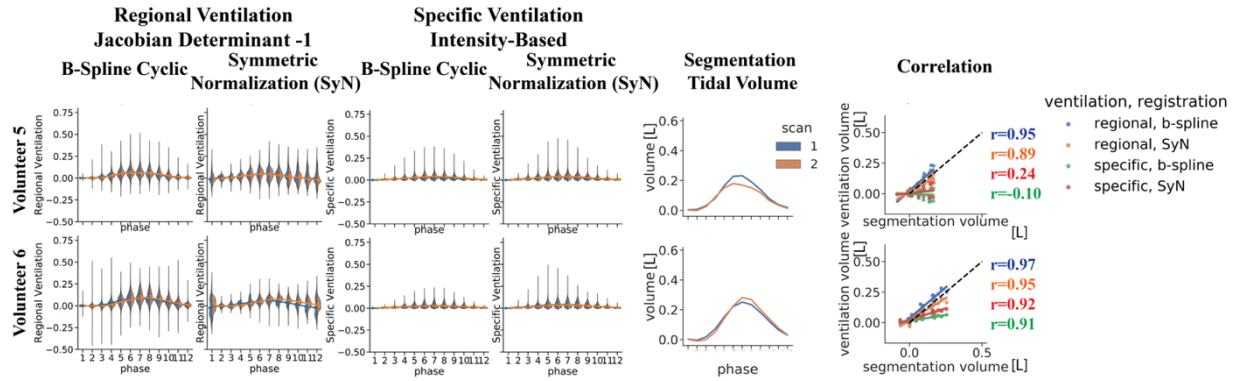
Figure 3.3 Split Violin Plot of the Ventilation Distribution, Segmentation Tidal Volume, and Their Correlation of Two Representative Subjects.

The discrete horizontal axis are the respiratory phases starting from end-expiration. In the split violin plots, the two colors represent the 1st and 2nd scan respectively, the shaded areas depict the distribution, and the solid line across phases is the median. As for correlation, the Pearson r values are color coded for each registration and ventilation combinations.

Figure 3.4 compares the total ventilation as measured by each method between scans across all volunteers and respiratory phases. The Bland-Altman plots show that b-spline registration with specific ventilation has the smallest variation yet also smallest range. There are increased differences between scans as total ventilation increases, which occurs at the respiratory phases closer to end-inspiration, phases 4-8.

19
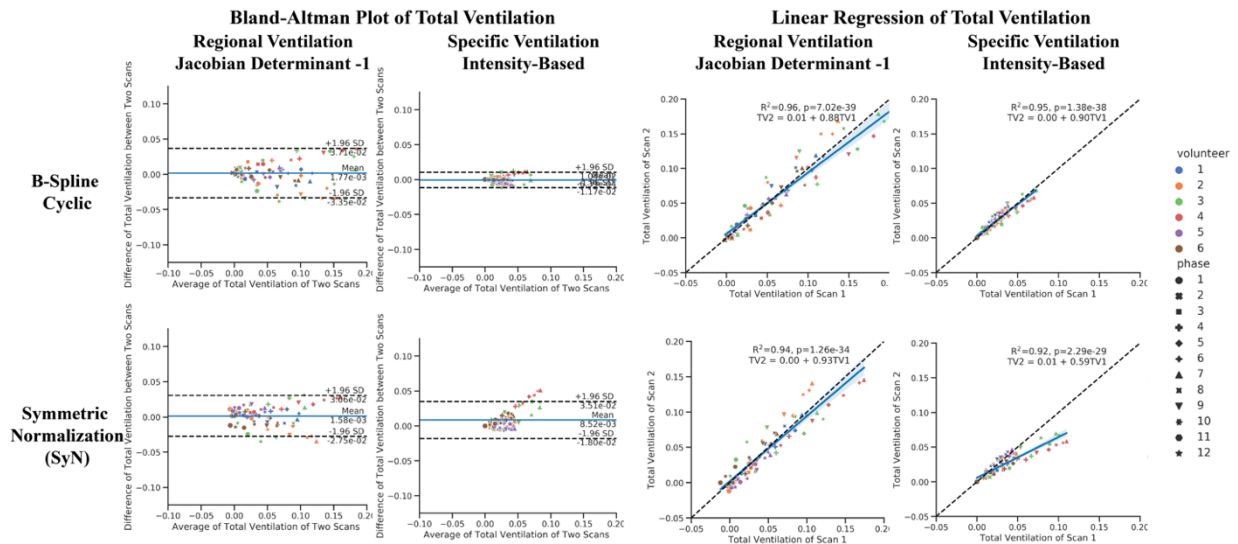
Figure 3.4 Bland-Altman Plot and Linear Regression of Total Ventilation across all subjects and respiratory phases.

The total ventilation is calculated by averaging all regional ventilation within the lung volume. Each color represents a volunteer while each shape represents specific respiratory phase.

The slopes of the linear regression lines of three methods, both regional ventilation methods and b-spline registration combined with specific ventilation method, are close to 1. They also showed higher correlations, with R^2 values 0.94-0.96. Total ventilation of Volunteers 1 and 6 align most with the dashed slope 1 line, which matches our observation from the split violin plot.

Sectional Ventilation

Figure 3.5 and Figure 3.6 show analyses of ventilation with lungs that are separated into six different zones, lower left, lower right, middle left, middle right, upper left, and upper right sections, to learn how different sections contribute to interscan variations. Results are shown only for the cyclic b-spline registration combined with the regional ventilation approach.
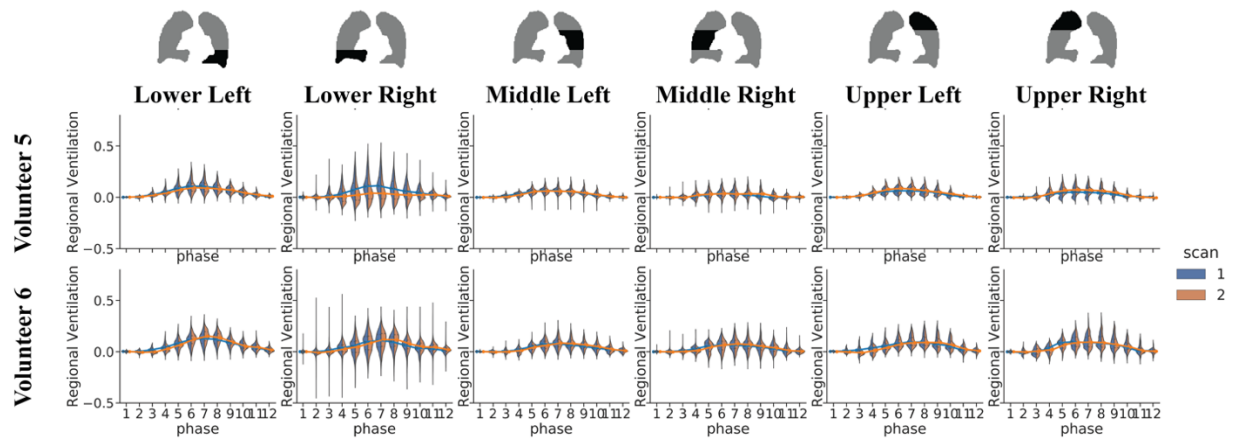
Figure 3.5 Split Violin Plots of the Ventilation Distribution for Six Lung Sections of Two Representative Subjects using the Cyclic b-Spline Registration and Regional Ventilation Method.

The subjects and the violin plot characteristics are the as Figure 3.3. The lower left and lower right regions have the highest median ventilation among all sections.
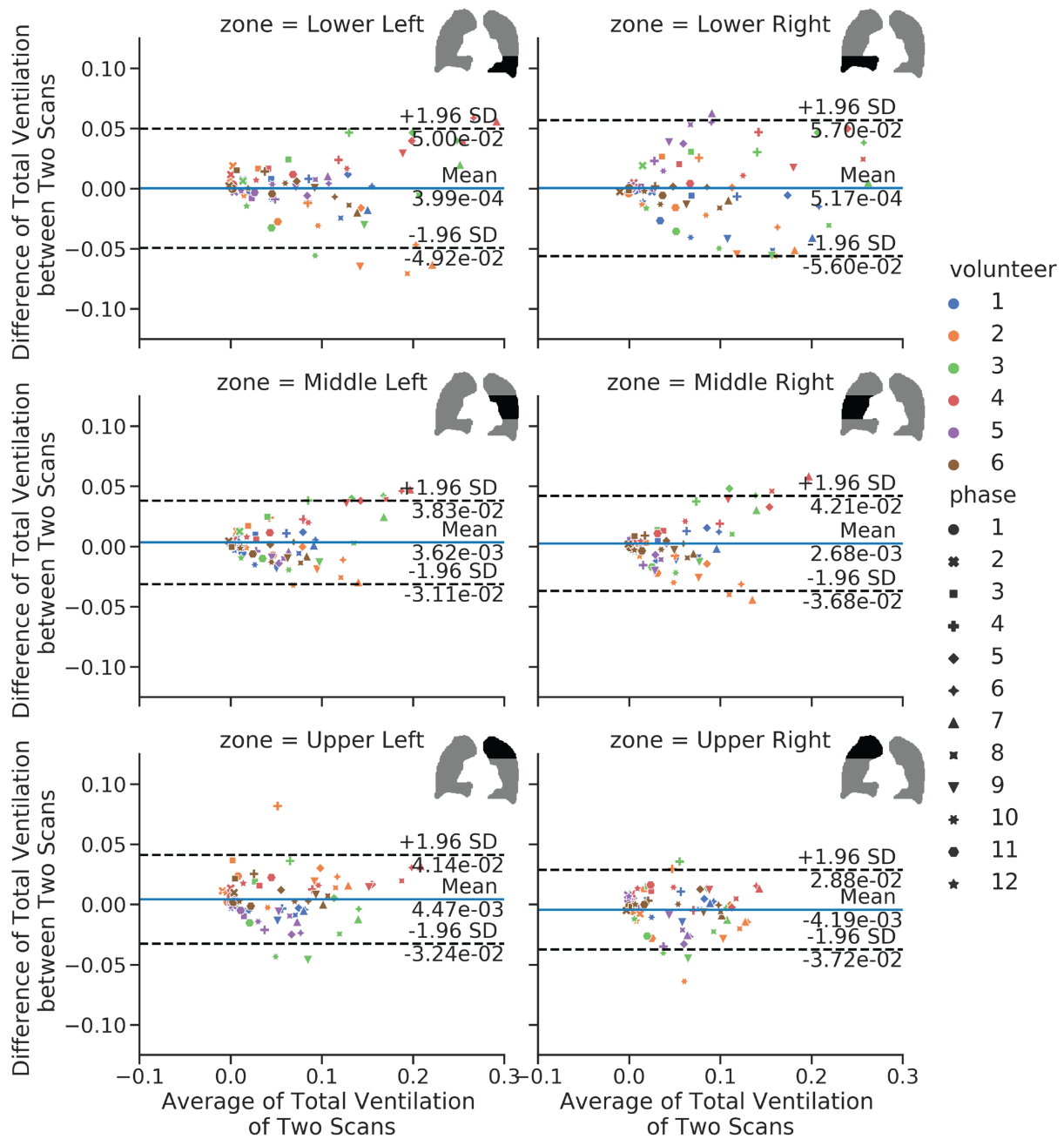
Figure 3.6 Bland-Altman Plot of Total Ventilation using the Cyclic b-Spline and Regional Ventilation Method.

The lower left and lower right regions have a larger span in average total ventilation of the two scans and a larger standard deviation in the difference between the two scans.

Table 3.1 Image-Based Pulmonary Function Measurements across all volunteers.

The respiratory rate is calculated from the filtered respiratory motion curve (Figure 3.1B), the functional residual capacity is the segmentation volume at the end-expiration state, and the tidal volume is the segmentation volume difference of the end-inspiration and end-expiration state.

	Volunteer	1	2	3	4	5	6
Respiratory Rate [breaths per minute]	Scan1	14.9±0.7	16.0±2.1	19.3±1.0	14.5±0.9	12.5±1.5	17.5±1.4
	Scan2	14.3±1.3	15.6±1.5	20.1±1.4	13.5±1.2	15.5±1.0	16.5±0.7
Functional Residual Capacity [L]	Scan1	3.85	1.59	1.91	2.14	3.37	2.77
	Scan2	3.60	1.58	2.00	2.14	2.75	2.88
Tidal Volume [L]	Scan1	0.46	0.18	0.40	0.52	0.32	0.26
	Scan2	0.43	0.27	0.34	0.38	0.12	0.29

3.4   Discussion

In this work, we implemented a phase-resolved reconstruction for radial UTE lung MRIs and calculated the ventilation maps. We tested four approach combinations, covering two registration methods, the 3D+t b-spline cyclic registration [33] and symmetric normalization [34], and two ventilation map quantification methods, the deformation field-based regional ventilation [39,40] and the intensity difference-based specific ventilation [41,42] method. Through violin plot, coefficient of variation, Bland-Altman plot, and linear regression, we observed different performances from these methods. The cyclic registration combined with regional ventilation has the highest correlation with segmented lung volume, while cyclic registration combined with specific ventilation was the most reproducible.

Regional Ventilation Versus Specific Ventilation

Based on our investigation, regional ventilation correlates better with segmentation lung volume, while specific ventilation is more reproducible.

We believe several factors might contribute to this performance. Since the intensity-based specific ventilation uses the image intensity, it is more sensitive to low SNR and image registration errors particularly from partial volume effects of vessel or chest wall signals that are much higher than the lung parenchyma. Because of this, spatial and temporal averaging is required for noise reduction. This improves the reproducibility yet leads to a smaller ventilation range as shown in the split violin plots in Figure 3.3.

The specific ventilation calculation also relies on the assumption that the MR signal is directly proportional to proton density, but this may vary due to T2* changes [8] and the coil sensitivity map changes caused by breathing. On the contrary, the regional ventilation uses Jacobian determinant of the motion fields, which is a direct measurement of volume change ratio. This could help explain that the regional ventilation correlates better with the segmentation lung volume.

The Effect of Registration Methods

We observed b-spline registration outperforms the SyN registration in both reproducibility and the ability to account for the cyclic nature of respiration by different registration methods.

As for cyclicity, we expect the concatenation of all motion fields from phase 1 to 12 back to phase 1 should be close to zero and thus has regional ventilation close to zero in phase 1. If we look at the ventilation colormap in the representative volunteer in Figure 3.5, the regional ventilation values for phase 1 using cyclic registration are close to zero which suggests this registration is enforcing cyclic behavior. While for SyN registration, the ventilation of phase 1 has a large range, showing that cyclicity is not accounted for.

This could be explained by the algorithms of the registration methods. 3D+t b-spline registration applies b-spline grids in the wrapped temporal dimension, which assumes the first and last temporal frames are adjacent. However, in SyN registration, since the motion fields are concatenated from phase 1 to 12, slight errors in each registration step accumulate, and thus the SyN method does not account for cyclicity.

Limitations

This study has a few limitations. First, we fixed the reconstruction to 12 respiratory phases, balancing between less streaking artifact and more respiratory phases. We speculate that with a smaller number of bins, the data to reconstruct each image will increase, leading to an increased SNR, which will potentially improve the performance of the intensity-based specific ventilation. Second, we tested one set of registration parameters on both registration methods. Second, we modified the b-spline cyclic registration parameters from [33] and the SyN registration parameters from ANTs default. The parameters were tuned by manually inspecting the quality of the registrations. However, some key parameters such as the multiscale registration levels, the grid

spacing, or the smoothing factor may affect the registration performance or the smoothness of the motion field. Thus, their effects on ventilation quantification need further investigation.

3.5 Conclusion

In this reproducibility study, we tested four combinations of registration methods and ventilation calculation methods to quantify ventilation on 3D phase-resolved ^{1}H UTE MRI of healthy volunteers.

We conclude that cyclic registration is superior to SyN for ventilation purposes. The registration method significantly affects the registration-based ventilation analysis. Regional ventilation correlates better with segmentation lung volume, while specific ventilation is more reproducible.

The sectional analysis implies that the lower left and lower right sections ventilate the most during MRI scanning and account for the most between-scan ventilation differences.

Chapter 4 Motion-Compensated Low-Rank Reconstruction (MoCoLoR) for Simultaneous Structural and Functional Ultrashort Echo Time (UTE) Lung MRI

4.1 Introduction

Proton ultrashort echo time (UTE) MRI has gained more attention recently in thoracic imaging because of its ability to capture fast relaxing signals with inherent motion management capabilities [43,44] and provide simultaneous structural and functional imaging [45]. However, due to the limited encoding speed of MRI, and the substantial data required for volumetric images, respiratory motion remains challenging for imaging in these anatomies. Conventional MR respiratory motion management techniques include breath-holding, respiratory triggering, and gating using signals from external devices such as a bellow or MR navigators [46–49]. While these approaches reduced motion artifacts, breath-holding limits the total scan time and increases patient discomfort. Respiratory gating methods suffer from prolonged scan time and low data efficiency.

3D non-Cartesian acquisition schemes such as 3D radial [50], cones [51], stack-of-stars [18], etc., can support robust respiratory motion management. These trajectories repeatedly acquire the center k-space, which serves as a self-navigator for respiratory gating. (Pseudo-)random ordering [52–54] can be easily incorporated into non-Cartesian acquisitions to increase temporal sampling incoherence. In addition, the ultrashort echo time minimizes the signal loss caused by the short

T2* from the air-tissue interface susceptibility, while radial acquisition samples k-space center first which preserves the low frequency signal, and thus increases the lung parenchyma signal.

One motion management strategy is motion-resolved reconstructions [4,55–60] that allows for continuous free-breathing acquisitions as well as pulmonary function analysis. These methods group the k-space data based on a motion signal and reconstruct the data into multiple respiratory states or time points using compressed sensing and parallel imaging techniques. For example, XD-GRASP [18] applies the total variation (TV) constraint along the motion states dimension. An alternative to the TV constraint is to reformulate the image series into a spatiotemporal Casorati [61] matrix, then enforce low-rank on the Casorati matrix. This approach is used in free-breathing cardiac MRI and dynamic contrast-enhanced (DCE) MRI [62–64].

Several methods for motion compensation have been introduced and demonstrated for lung MRI, including iMoCo [19] and MostMoCo [20]. In these methods, the motion fields are included in the data consistency term for an improved motion-resolved reconstruction. Other methods have integrated motion information into low-rank constrained reconstruction models, such as motion adaptive patch-based low-rank constrained reconstruction field [55,65] and block low-rank sparsity with motion-guidance reconstruction [66]. These methods preserve the low-rank property of spatiotemporal matrices by searching similar patches locally from the image series. Recently work on free-breathing cardiac MRI has demonstrated the ability to incorporate rigid and non-rigid deformations into the reconstruction along with a patch-based low-rank penalty [67], including for 3D radial trajectories [68].

A major application of motion-resolved lung imaging is pulmonary function analysis. Developments in proton MRI-based function analysis include Fourier Decomposition [69], PREFUL [70,71], and flow-volume loop [72]. These approaches utilize intensity-based specific ventilation [73] for localized lung volume function quantification. These methods are also fundamentally limited by the lung parenchyma SNR, which is low due to short T2* and low proton density, and thus will benefit from any improvements in efficient use of the acquired data.

In this work, we aim to improve simultaneous structural and functional lung imaging by reconstructing respiratory-resolved images from 3D-radial UTE MRI with a method that directly incorporates motion compensation in the low-rank constrained reconstruction model, named Motion-Compensated Low-Rank (MoCoLoR) reconstruction. This motion compensation formulation aims specifically to improve the efficiency of respiratory-resolved images by allowing data from all motion states to more effectively contribute during image reconstruction. This method was evaluated in pediatric and young adult patients with suspected lung diseases under free-breathing and without sedation. This population had a range of body size, breathing patterns, and compliance in the MRI scanner, and thus provides a challenging, real-world scenario in which to demonstrate the performance of MoCoLoR and other respiratory-resolved reconstruction methods for structural and functional imaging.

4.2 Theory

Motion-Compensated Low-Rank Constrained (MoCoLoR) Reconstruction

In motion-compensated low-rank constrained reconstruction (MoCoLoR), we aim to reconstruct motion-resolved images from free-breathing, continuously acquired k-space data. To achieve

this, we formulate the reconstruction as an optimization problem that includes data consistency across all respiratory phase states and a low-rank constraint that includes estimated motion fields to reduce the rank. This is addressed in the following optimization problem,

$$\underset{X}{argmin} \frac{1}{2}\|W(FSX - d)\|_2^2 + \lambda_L\|MX\|_* \quad (1)$$

In the data consistency term, W is the density compensation factor, F is the non-uniform Fourier Transform, $S = [S_i]$ are the sensitivity maps of coil i, $d = [d_{i,j}] \in \mathbb{C}^{B \times C \times bPE \times FE}$ are the binned data from coil i and respiratory state j, and $X = [X_j] \in \mathbb{C}^{B \times N^3}$ are the 3D images at respiratory state j. B is the number of respiratory states, C is the number of coils, bPE is the number of phase encodings or spokes per respiratory state, FE is the number of frequency encodings or readouts per spoke, N^3 is the image size. In the regularization term, $\|.\|_*$ is the nuclear norm, λ_L is the low-rank penalty regularization parameter, $M = [M_j]$ are the motion field operators.

During the iterative optimization, image X is updated in the inner loop and M is updated with image registration in the outer loop. The detailed iterative schemes, their derivation and a complexity analysis are included in the supplementary material.

Figure 4.1 summarizes the reconstruction theory of the MoCoLoR method. As shown in Fig. 1e, the addition of the motion compensation (MoCo) to the low-rank term reduces the apparent rank. When MoCo was applied, there is very little signal or structure in the 3rd and higher spatial bases derived from SVD, whereas without MoCo there was more visible signal and structure in the 2nd and 3rd spatial bases. This is a major motivation for this method.

a) Filtered Respiratory Signal & Data Binning

b) Binned k-Space Data

c) Data Consistency & Reconstructed Image

state 1 X_1 M_2 state 2 X_2 M_N state N X_N

Iterative Motion Field Update

d) Motion Compensated Regularization

time/ respiratory state

image space

spatial basis

SVD

temporal basis

$MX = [M_1X_1, M_2X_2 ..., M_NX_N]$ $MX = U\,S\,V$

e) spatial basis

w/o MoCo

w/ MoCo

U_1 U_2 U_3 U_4
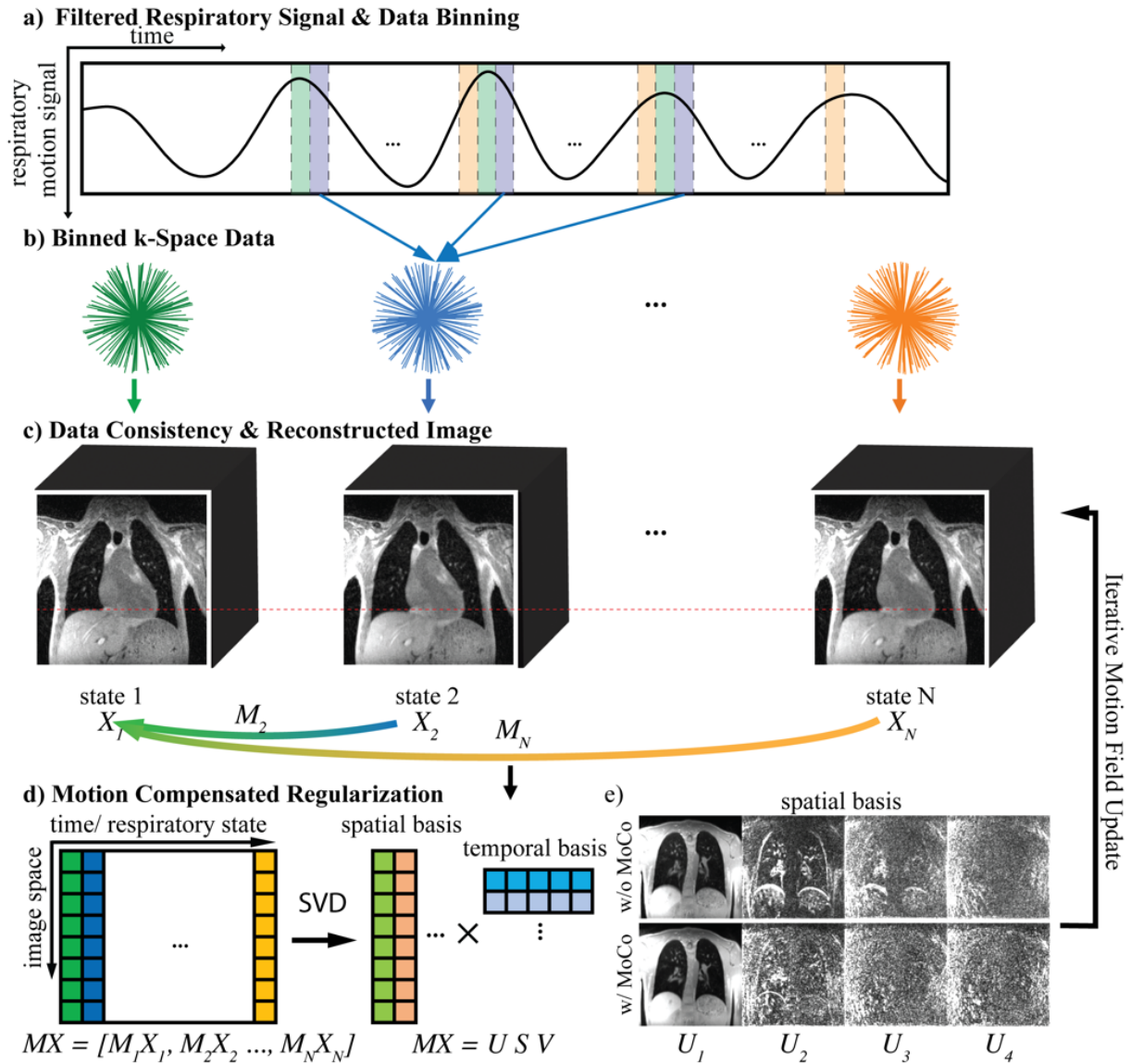
Figure 4.1 Motion Compensated Low-Rank Constrained (MoCoLoR) Reconstruction Workflow for Respiratory Phase-Resolved Lung MRI.

(a) First, a respiratory signal is required, which can be derived from the center of the k-space. (b) Based on this signal, raw data is grouped by respiratory states. (c) Respiratory phase-resolved image volumes are iteratively reconstructed by MoCoLoR, including image registration between respiratory states. (d) Singular vector decomposition (SVD) is used to enforce low rank. (e) A sample visualization of the spatial bases from SVD shows that adding in motion-compensation (MoCo) from the estimated motion fields compresses the information into fewer components, decreasing the rank. This framework can also be adapted to reconstruct time-resolved images.

31

4.3 Methods

Data Acquisition

All procedures were approved by the University of California, San Francisco Institutional Review Board. Written consent or assent was acquired from guardians or patients.

The study included eighteen datasets retrospectively from fourteen pediatric and young adult patients (4-25 y/o) clinical scans between 2018 and 2022. Three of them received repeated scans at different ages (5&5.5 y/o, 4&4.5&6 y/o, 14&16 y/o). The patient population covered a variety of lung conditions, including bronchiolitis obliterans (inflammation of the airways), nodules, and atelectasis (collapse of the lung). Inclusion criteria were patients that has high resolution (~1mm) radial UTE acquired during a clinical or research chest MRI, and were under the age of 18 or were being treated in the pediatrics department. A parent companion, video goggles, and audio headphones were adopted for the younger participants to increase patient comfort and cooperation. No sedation was administered. Throughout the UTE sequence, patients maintained a supine position and practiced free tidal breathing.

All data were acquired on 3T scanners (MR750 & MR750W, GE Healthcare, Waukesha, WI, USA) with an optimized 3D radial UTE sequence [26] with golden-angle ordering. The key parameters were flip angle = 4°, resolution = 0.9 - 1.5 mm isotropic, # spokes = 80,000 - 150,000, FOV = 24 - 40 cm isotropic, TE/TR = 0.07 - 0.10/2.8 - 3.8 ms, bandwidth = 125kHz, total scan time = 3'33" - 7'55". Depending on patient size, we used an 8-channel or 32-channel cardiac coil (GE Healthcare) or a 12 or 24-channel ultra-flexible chest coil [74] (Inkspace Inc.). A fast respiratory-gated reconstruction was available for image quality assessment at the scanner.

The resolution and FOV were chosen based on patient size, while number of spokes were selected based on the time available during the clinical scan.

All reconstructions for the proposed and comparing methods were performed offline on a Linux workstation, which had 200 GB memory and a 12 - 32 GB VRAM GPU. The SigPy package [75] was used for sensitivity calibration, GPU handling, and optimization. All reconstruction scripts are available on GitHub (https://github.com/PulmonaryMRI/MoCoLoR).

Respiratory Motion Estimation & Data Binning

The position in the respiratory cycle was estimated from the center of k-space of each radial spoke. DC signal from all coils was bandpass filtered separately by cutoff frequency 0.1Hz and 0.5Hz to reduce noise and separate the respiratory contributions from cardiac motion contributions. The filtered DC signal from the coil with the highest standard deviation represented respiratory motion. The peaks or local maximum of this respiratory motion curve were chosen to represent end-expiration. The detected peaks with a value smaller than the signal mean were excluded. The data points between two adjacent peaks were separated into R respiratory states in the time dimension, where each state contained the same number of data points (Figure 4.1 a).

The k-space data were then binned according to their corresponding time in the respiratory motion curve. The whole respiratory cycle was split into R states. R = 2 - 50 were tested on one representative patient due to computation time considerations, and R = 10 was selected for all

patients in this study. Details for the number of states selection were explained in the result section.

MoCoLoR Implementation Detail

The end-expiration state (State 1 in Figure 4.1 c) was selected as the reference state for motion field estimation because the end-expiration is lengthened in a regular breathing pattern. Thus the image in this respiratory state contains minimal within-state motion. Image registration for all approaches was performed using ANTs [34] deformable registration with the same parameters.

Due to computational time concerns, we tested the regularization parameter $\lambda_L = 0.001, 0.005, 0.01, 0.05, 0.1, 0.5$ for all three methods on a single patient. As explained in the results section, $\lambda_L = 0.05$ was selected for MoCoLoR. We didn't adopt coil for the proposed or comparing methods. The algorithm convergences were reported in the supplementary material. Based on the convergence, the number of iterations for XD Recon, MostMoCo, and MoCoLoR was selected as 25, 15, and 45, respectively.

Ventilation Quantification

Regional ventilation is derived from the registration motion field M. It measures the percentage of volume change during tidal breathing at each voxel. The definition of regional ventilation is as follows,

$$RV = \frac{V_{resp} - V_{end-expi}}{V_{end-expi}} = \frac{V_{resp}}{V_{end-expi}} - 1 = |det[Id + \nabla M]| - 1 \quad (4)$$

where V_{resp}, $V_{end-expi}$, are the lung volume at each respiratory and end-expiration state. Id is a 3-by-3 identity matrix, M is the motion field, ∇ is the Jacobian matrix, and det is the matrix determinant.

A regional ventilation value greater than 0 means lung tissue expansion, and less than 0 indicates contraction. The end-expiration state is selected as the reference frame where the ventilation is by definition zero. Region ventilation reports percentage of volume change instead of volume ratio in order to be directly comparable to specific ventilation.

The specific ventilation (SV) [76] is an intensity-based approach for ventilation quantification. It assumes that the signal intensity in lung parenchyma is proportional to the proton density, T1 is independent of air volume, and that mass is conserved. Specific ventilation is defined by the following equation,

$$SV = \frac{V_{resp} - V_{end-expi}}{V_{end-expi}} = \frac{S_{end-expi} - S_{resp}}{S_{resp}} \qquad (5)$$

where $S_{end-expi}$, S_{resp} are the signal intensity at each voxel in the end-expiration state and a respiratory image registered to the end-expiration image. The specific ventilation is truncated at zero for the ventilation map calculation to eliminate extreme values introduced by noise.

Lung segmentation

We adopted a 3D U-Net-based pre-trained neural network for lung segmentation [77] in its original form and weighting. 3D volumes at each respiratory state were processed separately. The lung masks maintained good visual quality and were used for ventilation map overlay.

Comparing Methods

For comparison, we reconstructed the data using the phase-resolved extra-dimension (XD) reconstruction proposed by Feng et al. [18]. In addition to the original total variation regularization in the temporal dimension, we added total variation in the spatial dimension for SNR improvement. The temporal regularization parameter $\lambda_t = 0.05$ and the spatial regularization parameter $\lambda_s = 0.01$ were selected based on a parameter search.

We also compared with the recent work on motion-state weighted motion-compensation (MostMoCo) reconstruction by Ding et al [20]. The temporal regularization parameter $\lambda_t = 0.05$ and the spatial regularization parameter $\lambda_s = 0.01$ were selected based on a parameter search.

Quantitative Analysis

Apparent SNR (aSNR)

Region of interest (ROIs) that covers the parenchyma, aorta, and trachea is manually drawn on a selected coronal slice that includes all structures. aSNR is calculated by $aSNR_{tissue} = \frac{mean(S_{tissue})}{std(S_{background})}$, where S_{tissue} is the signal intensity within the parenchyma, aorta or trachea, and $S_{background}$ is the signal intensity within the background [19]. The same ROIs are used across all three methods.

Maximum Derivative

The maximum derivative (MD) of the diaphragm is used to evaluate the sharpness of the image. A rectangular bounding box was manually drawn across the diaphragm of the selected coronal slice n at the end-expiration state. MD was measured by the maximum diaphragm gradient over

the mean liver signal among the 30 slices centered around slice n. A higher MD value represents a sharper diaphragm structure and indicates better motion correction improvement.

Paired t-test is used for significance analysis for apparent SNR and maximum derivative, where each data point represents one patient dataset.

4.4 Results

Figure 4.2 demonstrates representative reconstructed images and ventilation maps of the MoCoLoR approach in 14 y/o patient with severe combined immunodeficiency (SCID). We compared the structural image of XD Recon, MostMoCo reconstruction, and motion-compensated with low-rank constraint (MoCoLoR) reconstruction. The visualization of structures such as the pulmonary vasculature was similar across methods, but the XD Recon had slightly higher noise levels.

Regional ventilation and specific ventilation maps were also calculated. The end-expiration state is selected as the reference frame where the ventilation is by definition zero. The regional and specific ventilations vary with respiratory states, with the highest ventilation appearing at the expected end-inspiration state. The ventilation maps measured with the three reconstruction methods present similar patterns. The regional ventilation method in particular shows some potential ventilation defects near the base of both lungs. The specific ventilation maps have different ranges across the reconstruction methods, which likely is because XD Recon and MostMoCo regularize intensity differences, while the proposed MoCoLoR method regularizes

the absolute intensity values. Despite of the range difference, the ventilation maps show similar

patterns.
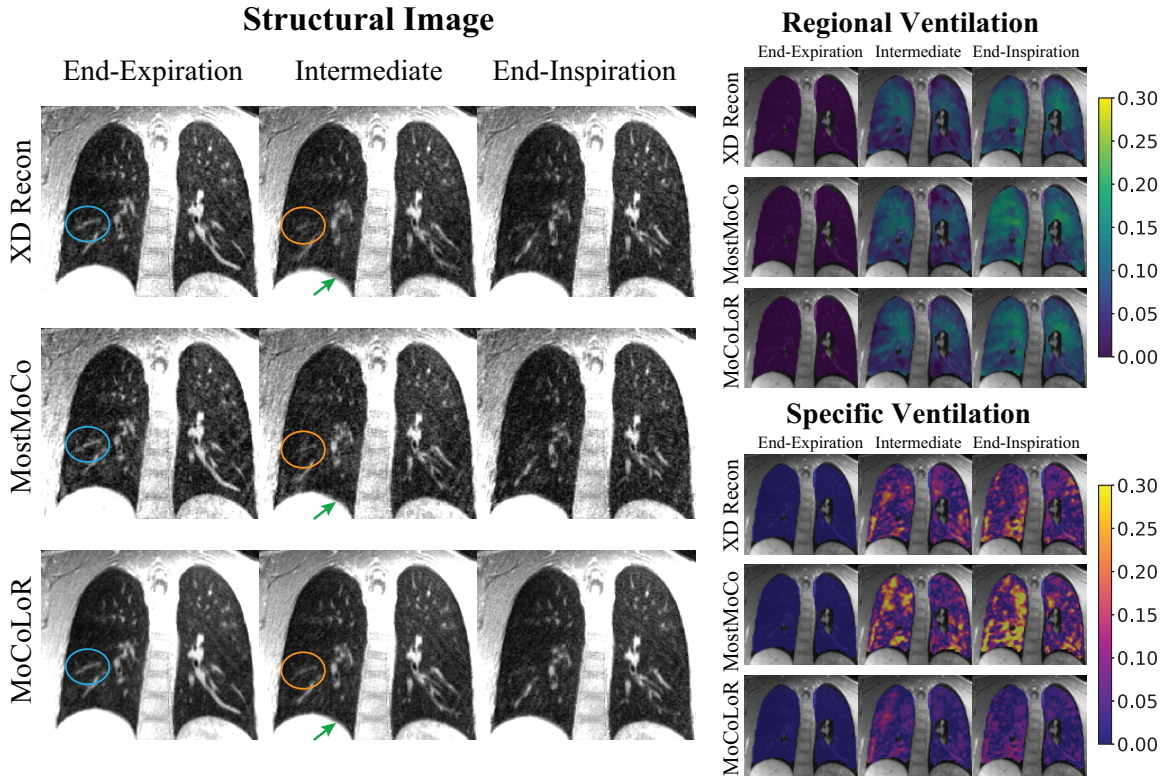
Figure 4.2 Representative Structural Image and Ventilation Maps.

The dataset represents a 14 y/o patient with severe combined immunodeficiency (SCID) who presented with dyspnea on exertion in different respiratory states. The circled regions show improved structures at end-expiration and intermediate respiratory states, and the arrows point to the sharpened diaphragm.

Figure 4.3 compares the apparent SNR and sharpness of all reconstruction methods for all

eighteen datasets, and a paired t-test is used for significance analysis. The aSNR box plots show

that the MoCoLoR methods yield higher aSNR in the parenchyma and aorta compared to XD

reconstruction and MostMoCo approaches. Since the trachea is filled with air, there's no signal

source, and in fact the aSNR should theoretically be zero in the trachea. According to the t-test,

all aSNR improvements were significant. The sharpness plot suggests that the MoCoLoR

approach has slightly decreased sharpness compared to the XD and MostMoCo reconstruction.
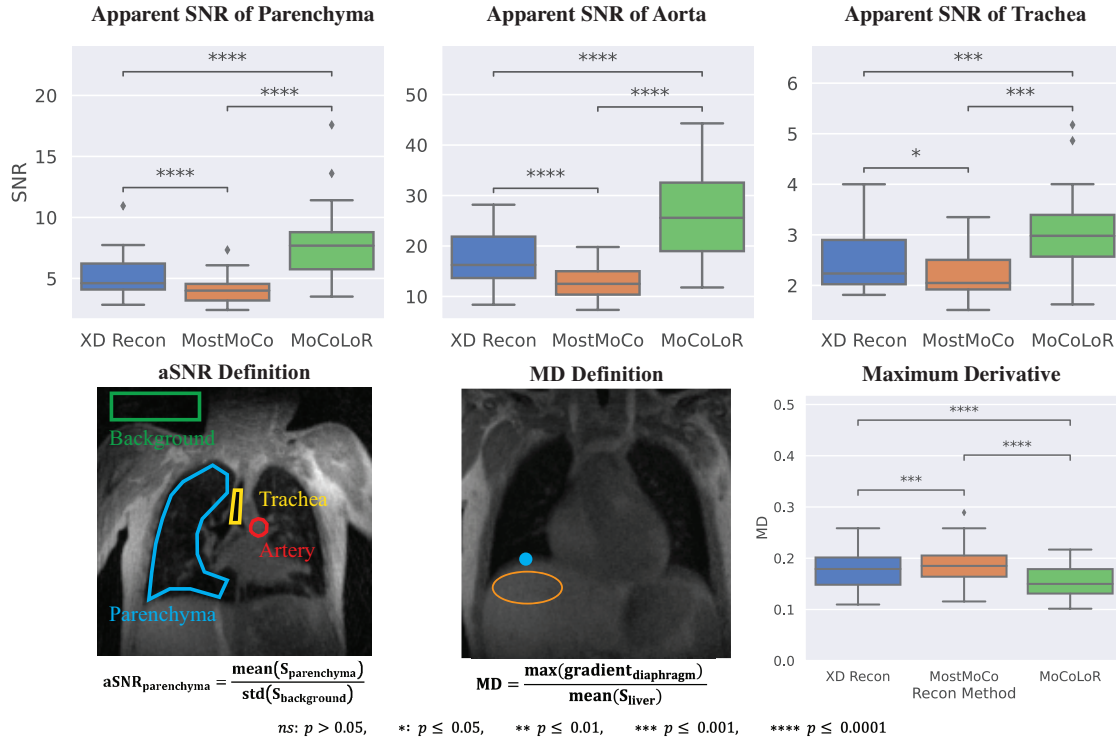
Figure 4.3 Box Plots of aSNR and Sharpness Measurements of All Datasets.

Apparent SNR (aSNR) of the lung parenchyma and aorta indicates an aSNR boost with the MoCoLoR approach. The Trachea aSNR measures the noise level within the trachea. Maximum Derivative (MD) of the diaphragm quantifies the sharpness. Mean and standard deviations are summarized in Table 4.1.

Table 4.1 Summary of apparent SNR and maximum derivative values

	Parenchyma aSNR	Aorta aSNR	Trachea aSNR	Diaphragm MD
XD Recon	5.31 ± 1.94	16.92 ± 5.41	2.53 ± 0.63	0.180 ± 0.040
MostMoCo	4.12 ± 1.32	13.20 ± 3.72	2.22 ± 0.49	0.192 ± 0.043
MoCoLoR	7.98 ± 3.52	26.18 ± 9.71	3.08 ± 0.96	0.159 ± 0.033

The effect of the regularization parameter on the reconstruction and ventilation analysis is summarized for a sample dataset in Figure 4.4. Among all the weightings for the nuclear norm λ_L, the highest aSNR appears at 0.05, 0.1 and 0.5. The regional ventilation appears over-smoothed when λ_L is greater than 0.1. Considering these trade-offs, we selected $\lambda_L = 0.05$ for the MoCoLoR reconstruction.
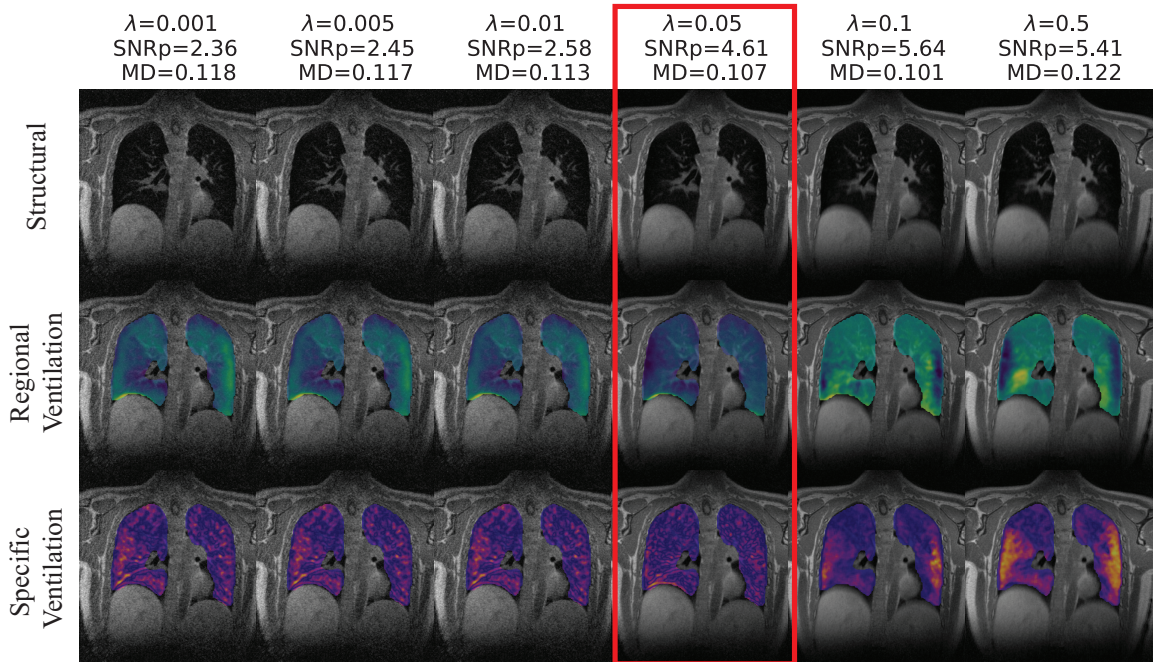
Figure 4.4 Investigation of the Regularization Parameter for MoCoLoR.

The figure depicts the structural and functional images of a 25 y/o patient with Leukemia. $\lambda_L = 0.05$ provides high parenchymal apparent SNR (SNR$_p$) and does not appear to over- or under-estimate the ventilation.

We further investigated the effect of the number of respiratory states on reconstruction and ventilation analysis in Figure 4.5 and Figure 4.6. Figure 4.5 shows a representative dataset where we reconstructed the dataset of 100,000 spokes into up to 50 respiratory states for all three reconstruction approaches. With the increased number of states, the diaphragm is sharper,

indicating that the respiratory motion is better resolved. There was no apparent loss in resolution or apparent SNR for up to 20 states, but 32 or more states present aliasing artifact. When separated into 50 states, MoCoLoR presented higher visual quality compared to the other two approaches.
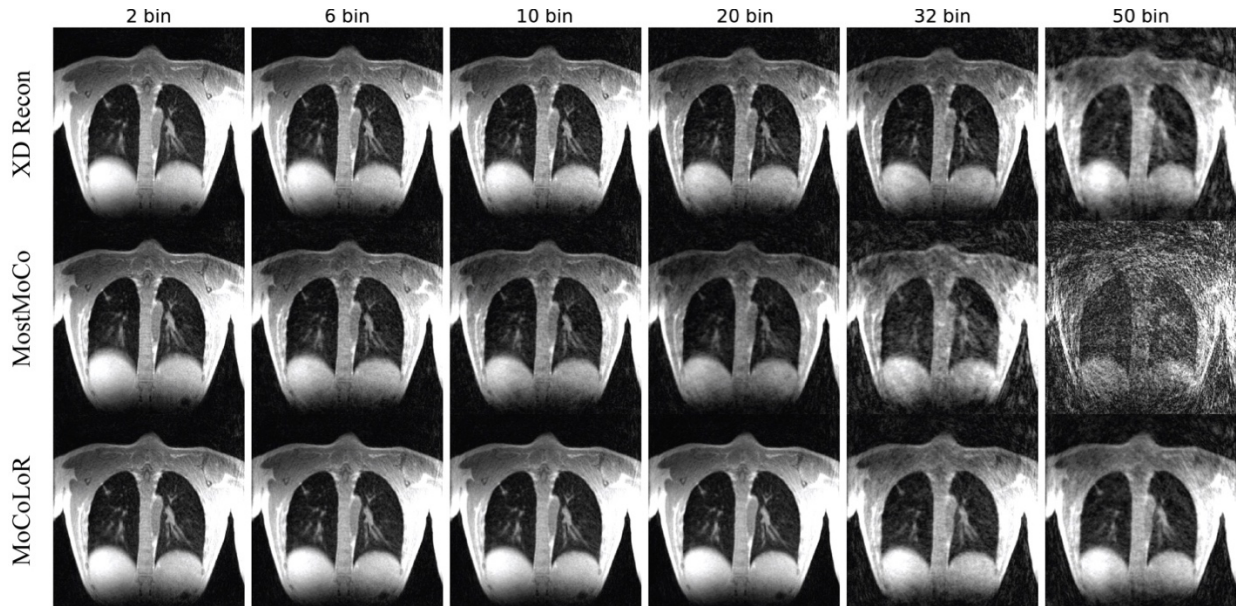
Figure 4.5 Number of Respiratory States of MoCoLoR.

One dataset from a 19 y/o patient with chronic cough and pulmonary nodules was reconstructed into 2-50 respiratory states. Structural images for 2, 6, 10, 20, 32, and 50 states were shown. The end-inspiration respiratory state was selected for illustration to demostrate the resolved motion blurring. With the increased number of states, the diaphragm is sharper while the aliasing artifact is more appearent.

Figure 4.6 quantifies the effect of the number of states on structural and ventilation imaging. For XD and MostMoCo reconstruction methods, aSNR decreases with the increased number of states. While for MoCoLoR reconstruction, aSNR first increases and then decreases with the increased number of states. Consistent with Figure 4.3, MoCoLoR had the highest aSNR of all methods between 6-20 number of states. The maximum derivative of MoCoLoR was slightly lower compared to the other two approaches. Note that the vertical axis of the MD diagram starts

at 0.14 to show the details, and MostMoCo did not converge in the 48-hour workstation grid job time limit and likely led to an unusually high value.

The number of motion states also affects ventilation measurements. We plotted the total lung averaged ventilation of one subject calculated from MoCoLoR. The regional ventilation converges with the increased number of states, remaining relatively stable at 6 states and above. A small number of states underestimate the ventilation at end-inspiration and other intermediate respiratory states. Specific ventilation also shows a trend of convergence but has greater fluctuations in some respiratory states between the reconstructions. Considering these aSNR and ventilation results, ten respiratory states were selected for all patient reconstructions.

Lastly, we investigated the structural images and ventilation maps from MoCoLoR in longitudinal lung MRI scans (Figure 4.7). A subject with interstitial lung disease received MRI at ages 4 and 4.5. The ventilation is normalized by the total percentage of volume change to account for the breathing depth difference. The histogram shows the normalized ventilation is more concentrated at age 4.5, suggesting a more uniform distribution of ventilation.
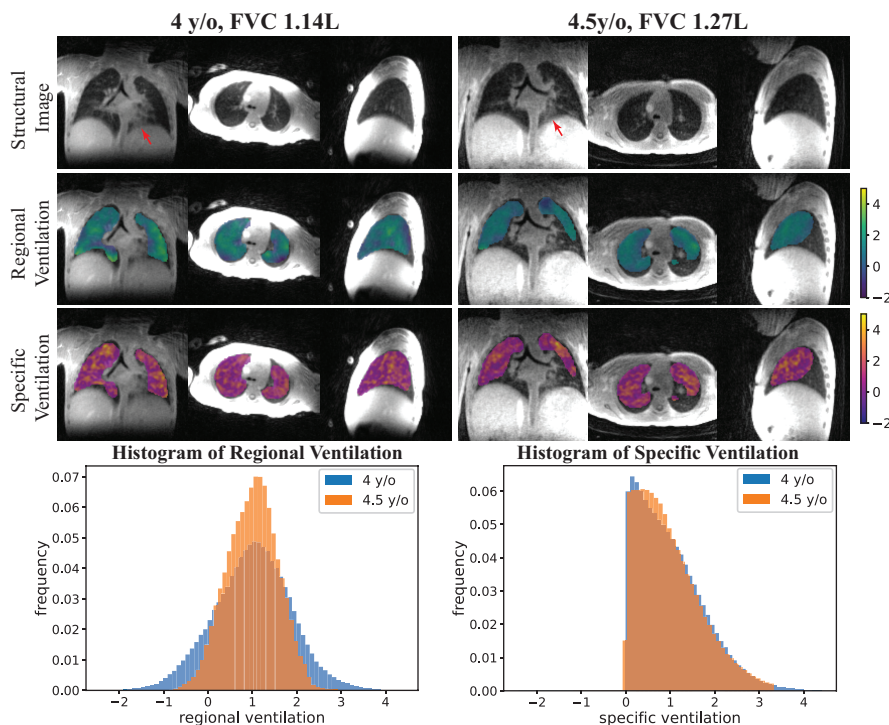
Figure 4.7 MoCoLoR Ventilation Mapping Applied to Longitudinal Imaging.

Repeated scans of a pediatric patient with childhood interstitial lung disease (ChILD) at ages 4 and 4.5 years old are shown. High-density suture material is visible in the left lower lobe at both time points (red

Figure 4.8 presents MoCoLoR reconstructed images at end-expiration state for all eighteen

patients included in the study. The datasets were acquired in a clinical setting and the parameters

varies with patient size, age, time available. This demonstrates that our technique is appliable on

a wide range of imaging parameters.

Figure 4.8 MoCoLoR Reconstructed Images at End-expiration State for All Eighteen Datasets. Images were enlarged to show details.

4.5 Discussion

This work demonstrates the feasibility of an image reconstruction method, MoCoLoR, that can simultaneously reconstruct high-resolution structural and functional images from a single 3D UTE sequence acquisition. This was evaluated in the extremely challenging scenario of pediatric patients, as young as 4 years old, who were all not sedated. All patients tolerated the scan well, and we were able to acquire the UTE sequence in a relatively quick approximately 5 minutes scan time. Structural images reconstructed with MoCoLoR showed improved apparent SNR compared to existing methods. The measured ventilation varies across respiratory states and converges to a consistent pattern with an increased number of states, which was chosen to be 10 for the lung UTE study.

In an exploratory longitudinal study with this approach, the ventilation maps reflected improved pulmonary function test results of the pediatric patient at different time points. The subject had improved forced vital capacity (FVC) from age 4 to 4.5, and the regional ventilation also showed improved uniformity.

In addition to respiratory phase-resolved imaging, the proposed MoCoLoR method was additionally able to produce time-resolved images in dynamic contrast-enhanced abdominal MRI. The results for DCE MRI were included in the Supplementary Material, showing the ability to produce time-resolved imaging with both respiratory and bulk motion correction in the MoCoLoR framework. This illustrates the flexibility of this approach, which we expect can also be applied to cardiac-resolved imaging as well with sufficiently high temporal sampling, cardiac motion signals (e.g. ECG, PG, navigators), and relevant contrast in the heart.

Total Variance and Low-Rank Constraints

The total variance regularization-based XD reconstruction is less computation-intensive than

MostMoCo and the proposed MoCoLoR method, which has the additional requirement of

motion state estimation. The reconstruction time comparison is in supplementary material.

MoCoLoR results, however, provide higher aSNR when more states are reconstructed.

Limitations

We acknowledge that there are some limitations to our work. First, while relative peak height

and width thresholding of the respiratory signal are applied to exclude irregular breathing, we did

not address bulk motion during the lung MRI scans. Fortunately, bulk motion was not observed

in most of our datasets, but this assumption can be challenging for the pediatric population.

However, a bulk motion correction term can be added to the MoCoLoR reconstruction

formulation, which we demonstrate in a pediatric 3D abdominal DCE MRI dataset in the

Supplemental Material. In this result, rigid bulk motion is estimated across bins in the temporal

(dynamic) dimension, and the resulting motion field is used for MoCo and the low-rank

minimization. The results show that 3 distinct periods of bulk motion were corrected and

improve depiction of the myocardium in DCE MRI. We could also minimize bulk motion by

using other means such as a weighted blanket and providing video distractions to subjects, or

through the use of image-based navigators for identification of bulk and/or irregular motion [4].

Second, the current image registration limits the speed of reconstruction. Image registration is

repeated in the reconstruction; however, the toolbox we adopted only supports CPU and not yet

GPU. We could further accelerate the algorithm by developing GPU-compatible registration.

Thirdly, there is a tradeoff between higher aSNR and higher sharpness (MD) for MoCoLoR approach, which is balanced by the regularization parameter. As for proton ventilation, although ground truth is unavailable in human subject studies, further validation is approachable. We plan to compare the proton ventilation results with the gold standard 129Xe MRI ventilation.

Finally, we did not include corrections for gradient non-linearity in this study. They will affect the regional ventilation in regions of gradient non-linearity. However, since the lungs are near the magnet isocenter and, especially for kids, do not likely extend into the highly non-linear gradient regions. For application of this method in clinical studies, gradient non-linearities can be incorporated as an image space correction using standard methods to correct this.

4.6   Conclusion

In conclusion, we demonstrated that a motion-compensated low-rank (MoCoLoR) regularized reconstruction approach can be used for simultaneous structural and functional lung MRI, even in challenging pediatric scans. The MoCoLoR reconstruction approach includes motion fields to reduce the rank and better share data across motion states during iterative reconstruction, which efficiently uses the data and results in high SNR in respiratory-resolved reconstructions. We evaluated this in pediatric and young adult subjects from ages 4-25 for radial UTE lung MRI acquired without sedation. With data from a 5-minute scan, the MoCoLoR reconstructions provided 1 mm isotropic high-resolution structural images as well as respiratory-resolved images. These were used in the lung at multiple respiratory states to compute ventilation maps at

the same high-resolution, where we observed anecdotal correlations between ventilation and lung function.

Chapter 5 3D Free-Breathing Ultrashort Echo Time (UTE) 1H Ventilation Compared with Hyperpolarized 129Xe Ventilation

5.1   Introduction

Imaging-based quantification of ventilation can provide critical information for the characterization of lung disease. While pulmonary function test only offers global information, MRI has the advantage of providing localized functionality. Respiratory disease patients, especially CF patients, can benefit from the ventilation maps MRI [78,79].

Noble gas MRI, such as hyperpolarized (HP) 129Xe MRI, can directly image the airspaces in the lung [80]. Since the inert gas only distributes in the ventilated regions of the lung, it has high contrast and serves as a gold standard for ventilation imaging. Several approaches have been proposed to quantify the 129Xe images. For example, Kirby et al. [81] introduced the k-means clustering approach for 3He and 129Xe gas MRI to compute the ventilation defect percentage (VDP). Alternatively, a linear binning approach [82] was proposed to quantify the 129Xe ventilation defect. Whereas 129Xe MRI requires specialized MRI equipment and is limited to a few specialized research centers worldwide, 1H UTE-based ventilation can be readily acquired on any MR scanner and therefore more readily available.

Proton MRI is easier to access but has yet to be widely used in pulmonary imaging due to the low proton density and high susceptibility at the air-tissue interface. Fourier decomposition [69] and PREFUL [70] enabled 2D ventilation quantification by acquiring consecutive 2D images during free-breathing and utilizing the intensity change at the respiratory frequency. 3D

ventilation and perfusion quantification methods such as SENCEFUL [83] were also proposed and have been validated in the CF population [79]. However, the lung parenchyma signal is not optimized, compromising the structural images' quality. Ultrashort-echo time (UTE) 1H lung MRI applies to structural image and ventilation map calculation. Motion-resolved reconstruction techniques can provide image volumes at multiple respiratory states by binning and jointly reconstructing the non-Cartesian raw data [4,18,20,45]. Ventilation can be calculated indirectly through the signal intensity change or regional volume difference between the states.

While the proton MRI is feasible for ventilation quantification, the correctness needs to be validated with existing methods. The previous analysis compared Fourier Decomposition (FD) 1H ventilation with HP 3He ventilation in COPD and Bronchiectasis population [84], PREFUL versus HP 129Xe in the CF population [85], UTE flow volume loop compared with HP 129Xe and PFT [86]. However, 3D UTE 1H ventilation based on regional volume difference still needs to be investigated against 129Xe MRI or PFT.

This manuscript compares the 3D UTE 1H ventilation calculated from motion-compensated low-rank constrained reconstruction (MoCoLoR) [5,6] with the HP 129Xe ventilation in healthy volunteer and CF populations for validation.

5.2 Methods

Participants

Twenty-four participants (ages 28.5 ± 14.7 y/o, 15 Males, 9 Females), including three healthy volunteers, six pediatric and fifteen adult subjects with cystic fibrosis (CF), were scanned

between February 2022 to August 2022 and were retrospective included in this study. The study was approved by the University of British Columbia Research Ethics Board (REB). Written consent/assent was acquired from all participants and guardians. The inclusion criteria were…

All participants have MRI acquired and are thus included in imaging analysis. Six subjects were excluded from the correlation with pulmonary function testing because PFT data were not acquired. Two additional participants were excluded from the correlation with the lung clearance index because the LCI was not collected. Figure 5.1 shows a flow diagram of the initial number of participants and excluded participants.
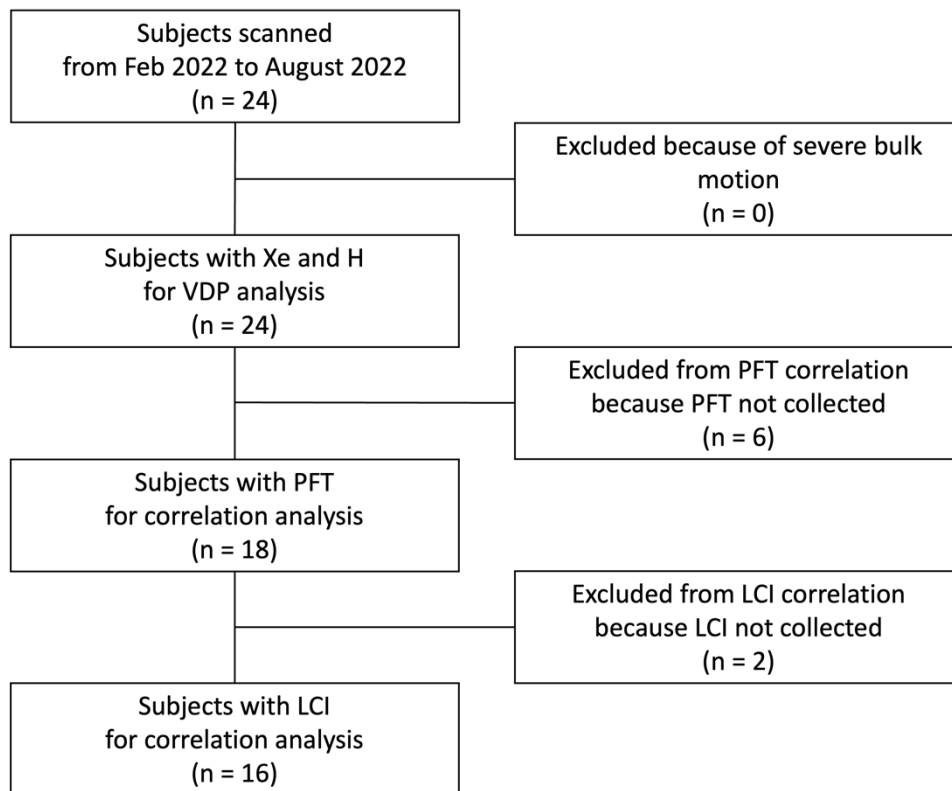
Figure 5.1 Flowchart of participant inclusion.

Imaging Protocol

Each subject inhaled hyperpolarized 129Xe/nitrogen gas mixture and went through a 2D multi-slice 129Xe spoiled gradient recalled sequence during breath-holding. Total inhaled gas and 129Xe doses were based on height [87]. Volume-matched 1H images were acquired using the body coil with room air inhaled. The two sequences were acquired with the same FOV = 40 cm × 30-40 cm, slice thickness = 15 mm, and the number of slices = 12-17.

A variable density 3D radial UTE sequence [88] was adopted for the UTE 1H acquisition during free-breathing. The key parameters were: FOV = 35 cm isotropic, resolution = 1.37 mm isotropic, number of spokes = 100,000, TE/TR = 0.07/2.88ms. All images were acquired on a 3T clinical scanner (Discovery MR750, GE Healthcare).

129Xe Ventilation Analysis

Xenon images for each subject were processed using the k-means method for ventilation defect quantification with an in-house developed MATLAB package [81,89]. Xenon images for each subject were separated into 5 clusters from the least to most ventilated (C1-C5) using a k-means clustering algorithm. The thoracic cavity was segmented from the 2D multi-slice 1H images using a region-growing approach. Lastly, the 1H images were registered to 129Xe, and the lowest cluster (C1) within the thoracic cavity was defined as ventilation defects. Ventilation defect percent was calculated as the ventilation defect volume normalized to the volume-matched 1H thoracic cavity volume.

UTE 1H Ventilation Analysis

Phase-resolved UTE 1H image volumes were reconstructed using the Motion-Compensated Low-Rank (MoCoLoR) approach [6]. Briefly, this method jointly reconstructs respiratory motion states with a low-rank penalty and uses iteratively refined deformable image registration between states to reduce the rank. Since it uses all data jointly in the reconstruction, it is very SNR efficient, similar to the iMoCo method [19]. Ten respiratory states were selected to balance the SNR and sharpness of the reconstructed image. Lung masks were segmented using a pre-trained U-Net neural network in ANTsPy [77]. The predicted lung masks were eroded by 3 pixels to reduce artifacts near the chest wall. After deformable image registration [90], the regional ventilation was calculated by the Jacobian determinant of the motion field at the end-inspiration state over the end-expiration state minus one. End-expiration state is the respiratory phase with the highest average regional ventilation signal, and the end-inspiration state is the respiratory phase with the lowest average regional ventilation. Regional ventilation at the end-inspiration state over the end-expiratory state forms phase-normalized regional ventilation. Lastly, the phase-normalized regional ventilation at the end-inspiratory state underwent a k-means approach for ventilation defect quantification, following the k-means for 129Xe [81]. Phase-normalized regional ventilation values are normalized to 0-255 and separated into k0 clusters. The cluster mean is initialized as the middle point of the equidistance ranges. For hierarchical k-means, an additional clustering was applied in the lowest cluster.

However, since the 129Xe and UTE 1H ventilations were acquired at different breathing maneuvers and presented different distributions, the k-means approach for UTE 1H ventilation needs to be modified. We tested four different clustering approaches, namely 1) simple k-means

into four clusters, 2) simple k-means into five clusters, 3) hierarchical clustering into four clusters (C2-C5), and then cluster C2 into four clusters (C21, C22, C23, C24). Combine C21 and C22 to form C1, C23 and C24 to form C2, 4) hierarchical clustering into four clusters (C2-C5) and then cluster C2 into four clusters (C21, C22, C23, C24). Combine C21 and C22, C23 into C1, and C24 into C2.

Figure 5.2 summarizes the 129Xe and UTE 1H VDP calculation pipeline.
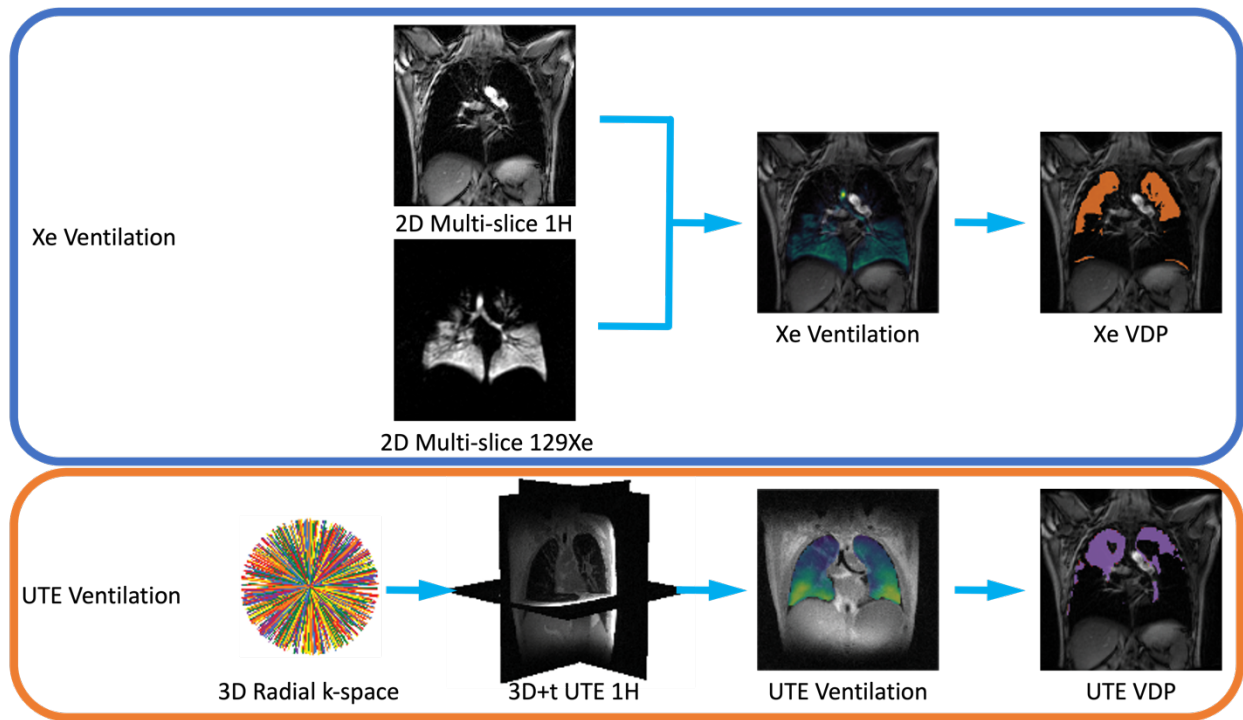
Figure 5.2 Image analysis pipeline

Pulmonary Function Test (PFT) and Multiple Breath Washout (MBW)

Eighteen participants underwent a pulmonary function test on the same day as MRI. The absolute values of forced expiratory volume during the first second (FEV1) and forced vital

capacity (FVC) were collected. The absolute spirometry measurement and demographics data served as input for percent predicted spirometry values. The predicted percentages were computed using the rspiro package v0.2 in R [91], following the Global Lung Initiative standard [92]. Sixteen participants underwent Nitrogen multiple breath washout for the measurement of lung clearance index (LCI). Correlations between each VDP (129Xe, UTE 1H) and each global function measurement (FEV1, FVC, LCI) were analyzed.

Statistical Analysis

The dice coefficient between the UTE 1H and 129Xe of the ventilated and ventilation defect area were combined to evaluate the accuracy of the segmentation. Specifically, we registered the 3D UTE 1H images to 2D multi-slice volume-matched 1H images using ANTs, which allows us to compare ventilated directly and ventilation defect segmentations. The dice accuracy was computed using the following equation,

$$Accuracy = DSC_{Ventilated} + DSC_{Ventilation\ Defect}$$

$$= 2 \times \frac{Area\ Xe_V \cap Area\ Xe_V}{Area\ Xe_V + Area\ Xe_V} + 2 \times \frac{Area\ Xe_{VD} \cap Area\ Xe_{VD}}{Area\ Xe_{VD} + Area\ Xe_{VD}}$$

Linear regression was used to compare the VDP calculated from 129Xe and UTE 1H and between VDP and global lung function measurements. Spearsman's correlation coefficient (r) and p-values were reported for linear regression. Bland-Altman plots were applied to compare the VDP derived from 129Xe and UTE 1H.

Box plots compared VDP values in healthy controls and CF patients. The median, 25th, and 75th quartiles were presented in the box plots. T-tests were used for linear regression to evaluate if the two data are correlated and if the healthy and respiratory diseased groups can be differentiated, where $p < 0.05$ is considered significant.

5.3   Results

Figure 5.1 plots the flowchart of the participants included in each analysis stage. All twenty-four subjects had MRI available and were included in the VDP analysis illustrated in Figure 5.4 & Figure 5.6. The comparisons between VDP and PFT were based on eighteen participants, as shown in Figure 5.5 a and b, while Figure 5.5 c is based on the sixteen participants who had LCI available.

Table 5.1 lists the demographics of participants enrolled in this study. Twenty-four subjects were included: three healthy volunteers and six pediatric and fifteen adult patients with cystic fibrosis (CF).

Table 5.1 Participant Demographics, Imaging, and Pulmonary Function Testing

	All	Healthy	CF
Demographic information			
Age (years)	29 ± 15		
Gender	15 M, 9 F		
Imaging	n = 24	3	21
129Xe VDP (%)	9.0 ± 9.5	0.3 ± 0.2	10.3 ± 9.5
UTE 1H VDP (%)	12.7 ± 4.1	9.1 ± 1.2	13.2 ± 4.1
Spirometry results	n = 18	0	18
FEV1 (%)	77.3 ± 18.4	NA	77.3 ± 18.4
FVC (%)	88.9 ± 7.0	NA	88.9 ± 7.0
FEF 25%-75%	57.0 ± 38.1	NA	57.0 ± 38.1
MBW results	n =16	1	15
LCI	9.0 ± 3.8	6.2	9.2 ± 3.9

Figure 5.3 illustrates HP 129Xe ventilation, UTE 1H structural image and ventilation, and VDP overlay of three representative cases. The cases were selected to demonstrate results from low, medium, and high Xe VDP, corresponding to healthy, mild, and severe ventilation defects. For the healthy subject (Figure 5.3 a), 129Xe circulated to all regions within the lung. UTE 1H also showed a uniformly distributed ventilation map with values greater than zero. As shown in Figure 5.3 b, the UTE 1H ventilation defect overlaps with the 129Xe ventilation defect at the superior and inferior lungs. For the subject with severe ventilation defect, the defect segmentations from 129Xe and UTE 1H have significant overlap areas, as indicated by the blue

area. UTE 1H correctly predicted the ventilation defects on the left and right middle and superior regions. Ventilation results from a patient with a mild ventilation defect. The structural images in all three coordinates have a high 1.37 mm isotropic resolution and can be used for radiology reading. The main distinction from previous methods is the ability to provide both high-quality structural images and functional maps.
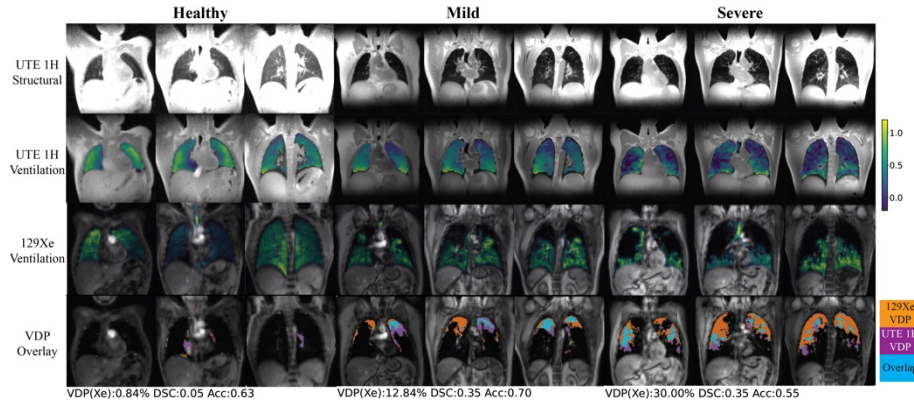
Figure 5.3 Representative Xe ventilation, UTE structural and ventilation map, and VDP overlay.

Figure 5.4 a demonstrates the dice spatial accuracy of the ventilated and ventilation defect region segmentation. Accuracy is defined as (overlapped ventilation defect region + overlapped ventilated region)/total lung volume. This metric mitigates the dice coefficient's strong dependency on the actual VDP value. The accuracy of UTE 1H was a mean of 0.63±0.05. Note that this accuracy value is susceptible to minor differences in image registration, which is challenging given that there was typically some motion between Xe and UTE scans. Figure 5.4 b plots the relationships of the VDP between 129Xe and UTE 1H across all subjects. According to the correlation plot, 129Xe VDP and UTE 1H ranged from 0 to 0.35. The VDP from 129Xe and UTE 1H positively correlate, with R-squared equal to 0.64. P-value = 0.02 further confirmed that the linear relationship is significant. Figure 5.4 c The Bland-Altman plot suggests a bias of -0.02

and limits of agreement of 0.14. No systematic differences were observed between the two methods.
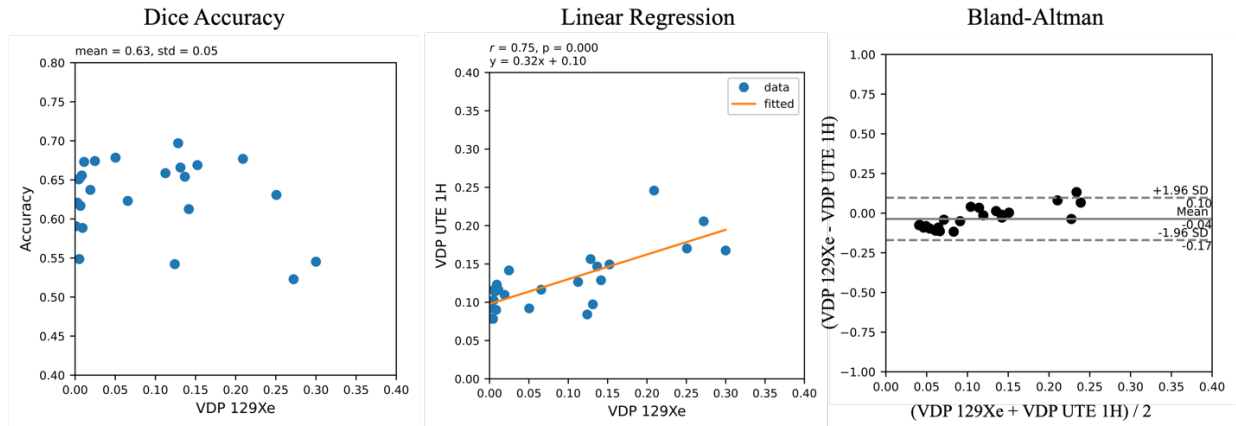
Figure 5.4 Dice Accuracy, Linear Regression and Bland-Altman plot for k-means Xe and H VDP.

Figure 5.5 plots the correlation between the results of image-based VDP (129Xe and UTE 1H) and global lung functional test (FEV1, FVC, LCI). 129Xe VDP and UTE 1H VDP both demonstrate significant negative linear relationship with FEV1, with p-value 0.003 and 0.016 respectively. The slopes are both negative, consistent with the high percentage of FEV1 corresponding to low VDP. UTE 1H presents a smaller absolute slope resulting from the smaller range of UTE 1H VDP compared with 129Xe VDP. The VDP UTE 1H is strongly correlated with the FVC, with p-value=0.005. This could be because both FVC and 1H UTE measure volume changes. FVC measures the global volume difference from fully inhaled to fully exhaled states, while 1H UTE regional ventilation measures the tidal volume change. 129Xe VDP strongly correlates with LCI, which confirms the previous findings (1). These findings suggest that UTE 1H ventilation is a good indicator of lung function and measure different function aspects compared to 129Xe ventilation.
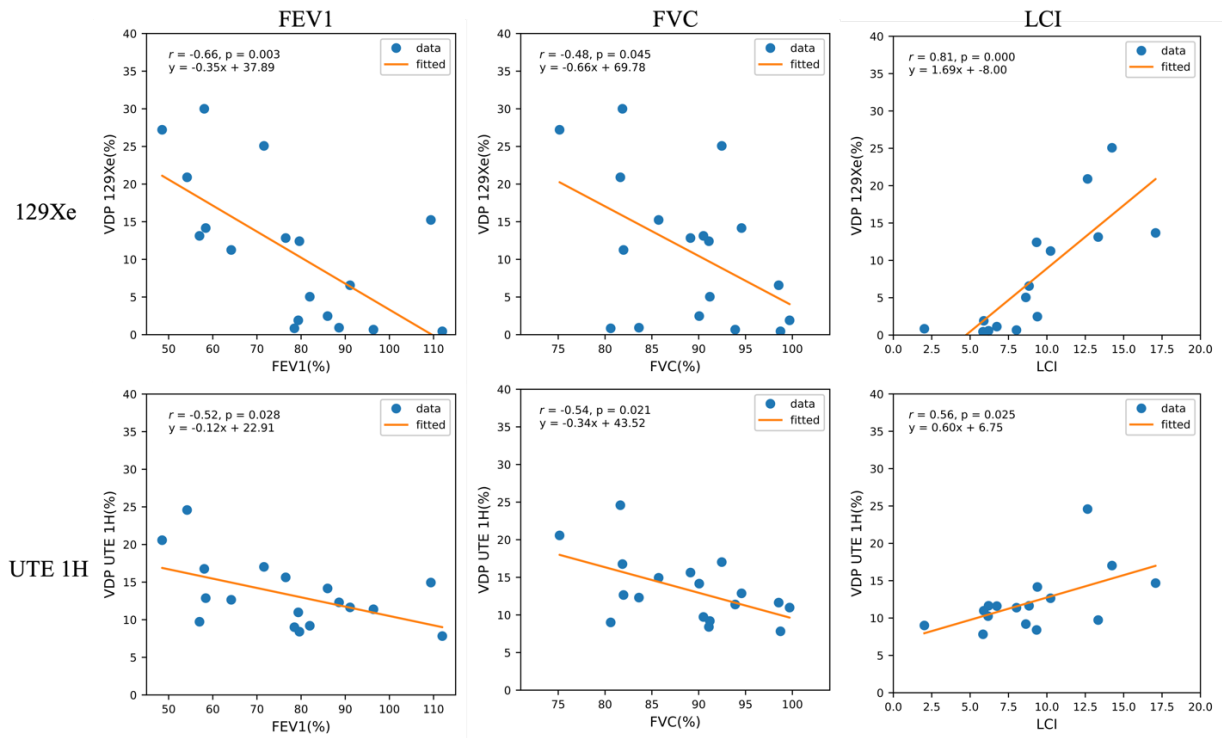
Figure 5.5 Correlation of Xe, UTE H ventilation and pulmonary function test results.

Figure 5.6 shows box plots of 129Xe VDP and UTE 1H VDP for healthy control and respiratory disease patients. 129Xe can distinguish respiratory disease participants from healthy controls. The median value for respiratory disease patients is 12.3, 25th and 75th percentiles are 11.0 and 14.9. The healthy control shows a median value, 25th and 75th percentile of 0.29, 0.19, and 0.40. UTE 1H VDP also had a difference in median value in patients and healthy controls. Comparisons for PFT and LCI were not investigated because there is no PFT and only 1 LCI for healthy volunteers.
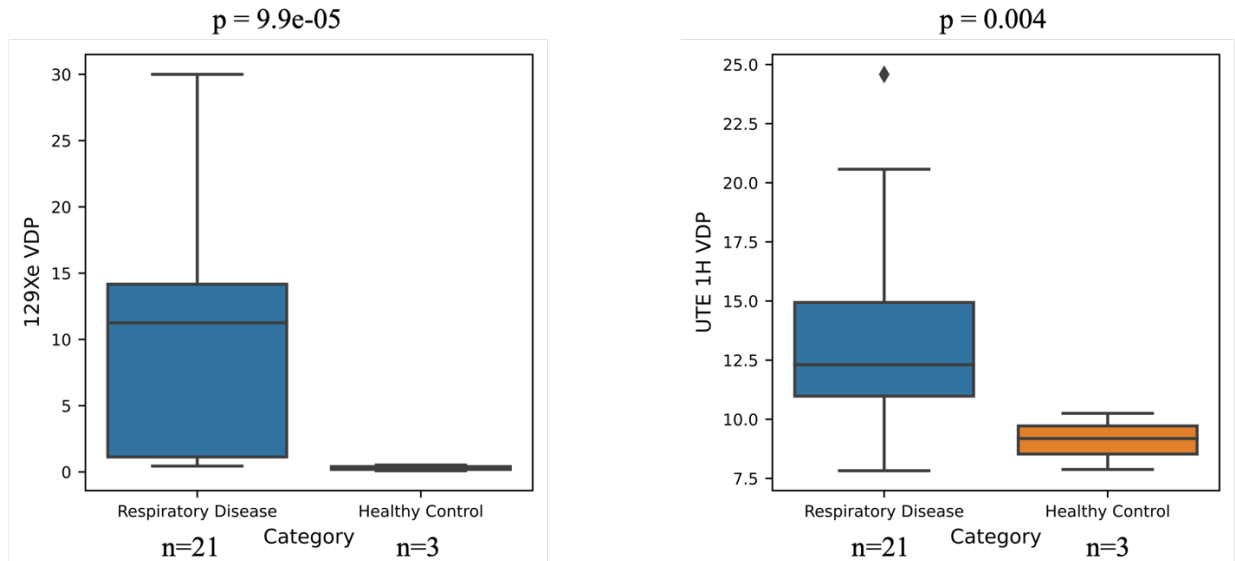
Figure 5.6 Box plot of Xe, H VDP in respiratory disease and healthy control participants.

5.4 Discussion

This paper demonstrated that UTE 1H ventilation from MoCoLoR positively correlates with the 129Xe ventilation with moderate-to-high accuracy for VDP quantification between the two methods. UTE 1H VDP also correlated with FEV1, FVC, and LCI, suggesting it is a valid biomarker for pulmonary function. The UTE 1H VDP had different ranges in healthy volunteers and respiratory disease subjects, indicating the potential for clinical application. Compared to PFT and 129Xe, UTE 1H provides localized ventilation information and can be performed at any site with an MR scanner without special equipment.

129Xe VDP vs. UTE 1H VDP

While 129Xe VDP and UTE 1H VDP are strongly correlated, range differences exist, and ventilation defect segmentation are not identical. We note that these two methods quantify ventilation in different respiratory maneuvers. UTE 1H is acquired dynamically during 5-min

tidal breathing. In contrast, Xe is acquired during a static ~10s breath-hold of a fixed volume from functional residual capacity. In addition, since the UTE 1H ventilation is an indirect measurement, a lower value could also reflect changes in increased stiffness/decreased compliance of that lung region. These factors may contribute to the difference in ventilation defect regions.

The two approach also demonstrates difference in the correlation with global function measurements. 129Xe VDP is better correlated with LCI which is a measurement for lung heterogeneity. UTE 1H VDP is better correlated with FVC, which is a measurement of the volume change. In addition, 129Xe is more sensitive in distinguishing healthy subjects and respiratory disease patients.

The requirements for acquisition are also different. 129Xe acquisition requires a volume-matched 1H for structure reference and registration. Participants need to inhale hyperpolarized 129Xe gas mixture and hold their breath during the scan. 1H UTE does not require special equipment and acquires during tidal breathing, thus rely minimally on patient effort. However, it can also be challenging for the pediatric subjects to stay still.

Advantage of UTE 1H MRI

The ability to provide simultaneous structural and functional information is a crucial advantage of 3D UTE 1H. The structural and functional images, and segmentations, are reconstructed or processed from the same sequence. No additional registration is needed across the

structural/functional images, and they can provide complementary information for clinical decisions.

In addition, the resulting 3D volume also allows multi-plane reformation of the data. Although 2D multi-slice pulmonary ventilation maps are commonly acquired and visualized in the coronal plane to address respiratory motion and minimize in-plane motion, radiologists are more accustomed to reviewing axial slices. For UTE 1H, the structural and functional maps can be reformatted into axial planes or other planes of interest, providing flexibility and accessibility during clinical application.

Limitations

We acknowledge that there are some limitations to our work. One limitation is the imperfection of the automated segmentation for 3D UTE 1H. The algorithm sometimes had difficulty near the chest wall or large vessels. Due to the vast amount of data in 3D volumes, manual correction of the segmentation can be challenging. To mitigate this problem, we implemented morphology erosion to include regions within the lung for ventilation analysis. However, the imperfection of the segmentation introduced a noise floor for ventilation defects and caused non-zero VDP in healthy volunteers.

Another limitation is the small number of healthy controls included in the study. Since this study is retrospective, the number of healthy participants and respiratory disease patients were not age or gender matched. Considering the resources needed for clinical study, we had limited healthy control participants who underwent 129Xe MRI, PFT, and MBW procedures.

5.5 Conclusion

In conclusion, we validated 3D UTE 1H ventilation against 129Xe ventilation and pulmonary function testing. It demonstrates a positively correlated VDP with the gold standard 129Xe and a high spatial VDP accuracy. It also showed a linear correlation with FEV1, FVC, and LCI. UTE 1H MRI ventilation may be implemented on any MR scanner and has the potential to be widely implemented to provide clinically relevant ventilation information for patients with lung disease. Future directions include application in other pulmonary diseases, improving image segmentation, and investigating other biomarkers developed from 1H MRI.

Chapter 6 Iterative Motion-Compensated Reconstruction with Convolutional Neural Network (iMoCo-Net) for Ultrashort Echo Time (UTE) Proton Lung MRI

6.1   Introduction

Proton pulmonary MRI is challenging due to the respiratory motion and low proton density. Breath-holding minimizes the motion but may not be tolerated by patients with severe diseases and the pediatric population, and also limits the spatial coverage and resolution due to the limited scan time. Free-breathing UTE sequence can produce high-quality proton lung MRI because it is more motion-robust compared to Cartesian sequences and exploits the fast-decaying signal. Motion-compensated reconstruction techniques [4,18,20,93] better manage respiratory motion for UTE acquisitions and are also more SNR efficient than respiratory-gated techniques. However, these methods are usually iteration-based optimization algorithms and can easily take hours to complete for a single dataset.

Meanwhile, technologists prefer visualizing the reconstructed image during scanning to validate if a repeated scan is needed, and radiologists usually read the images within 1-2 hours from the scan. An accelerated motion-compensated reconstruction is needed. Luckily, machine-learning approaches can meet this demand. Among the established networks, U-Net [94] is well suited for image reconstruction and motion artifact removal tasks. While the training process is time-consuming, the inference for one subject only takes a minute. This abstract explores the

feasibility of machine learning-based motion-compensated reconstruction for free-breathing UTE lung MRI.

6.2   Methods

Data Acquisition

Twenty subjects were retrospectively included in this study, ranging from healthy volunteers to pediatric and adult patients with lung diseases. Each subject underwent a 5-min free-breathing optimized radial golden angle UTE sequences [31] on a 3T clinical scanner (GE Healthcare, Milwaukee, WI) with a phased array coil. Key parameters were: resolution=1-1.5 mm, #spokes=80,000-100,000 spokes, TE/TR=0.07-0.1/2.7-3.8 ms.

Data Preparation

In order to form the network input, the raw data were separated into eight bins and reconstructed with Non-uniform Fourier Transform (NuFFT) reconstruction. The center of k-space was frequency filtered to track the respiratory motion for binning. Each motion state image corresponds to one input channel. We tested two sets of input, motion-resolved images reconstructed with all k-space spokes and the other mimicking an accelerated scan with only 50% of the spokes.

Iterative motion-compensated (iMoCo) reconstruction [19] results using all spokes were used as the target output for both cases. Depending on the number of coils, iMoCo reconstruction takes 1.5 to 6 hours to complete on our GPU server.

Center coronal slices that contain body structures were extracted as input and target images of the network. They were spatially normalized to matrix size 256x256, and the intensity was normalized to 0 to 1. The twenty data sets were separated into 16/2/2 patients for training, validation, and testing.

Network Structure

A 2D U-Net [94] was applied for the motion compensation task. Each encoding block includes a 3x3 padded convolutional layer, a rectified linear unit (ReLU) activation layer, and a batch normalization layer. A 2x2 max-pooling layer was applied between resolution scales. Similarly, convolution and ReLU layers were applied in the same scales for the decoding blocks, and a 2x2 up convolution was used between scales. The network was implemented in Tensorflow Keras with the mean absolute value error (L1) loss function and 50 epochs.

All processes, including data preparation and network training, were done on a GPU cluster, allocating one GPU (16 GB) core per task. The network structure details are summarized in Figure 6.1.
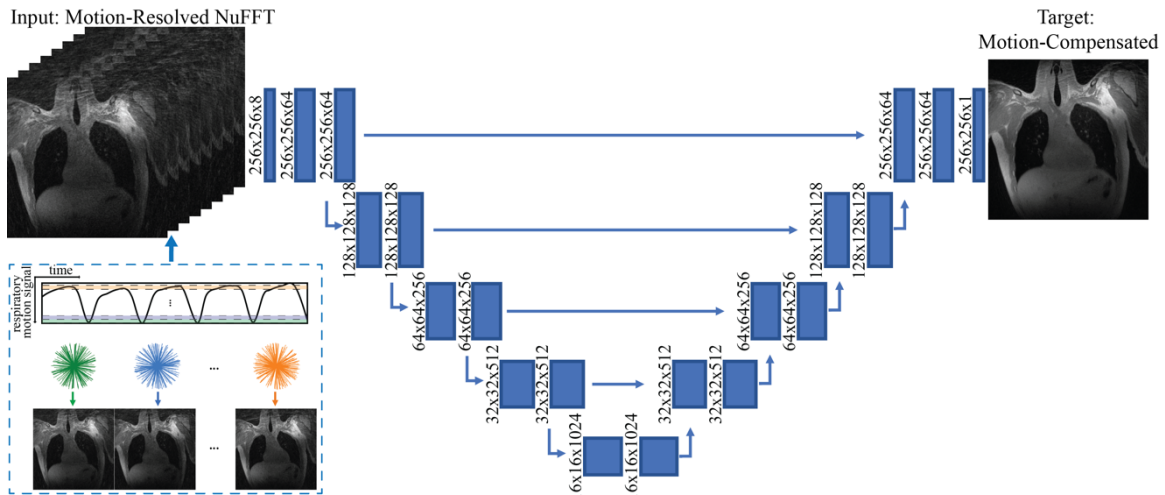
Figure 6.1 iMoCo-Net structure.

The inputs are motion-resolved images reconstructed with NuFFT, binned based on k-space center data, and the target output was the iMoCo reconstructed image.

6.3   Results

Figure 6.2 and Figure 6.3 demonstrate two example test set results from the neural network. The predicted image from all spokes preserves the fine vasculature structure of the lung. We also observe a sharper diaphragm and a higher apparent SNR compared to the averaged input. This indicates the network is successfully performing motion compensation and leveraging data from all motion states. As for the 50% spokes input, the prediction is significantly improved from the input but appears blurrier compared to the 100%-spoke results. The total reconstruction processing time for one subject is the time for NuFFT reconstruction (4 mins) and the time for inference (1 min for ~300 slices).

| Averaged Input | Predicted | Target | Difference |

100% spokes

SSIM 0.85, pSNR 26.21, MSE 2.39e-3

50% spokes

SSIM 0.81, pSNR 23.45, MSE 4.52e-3
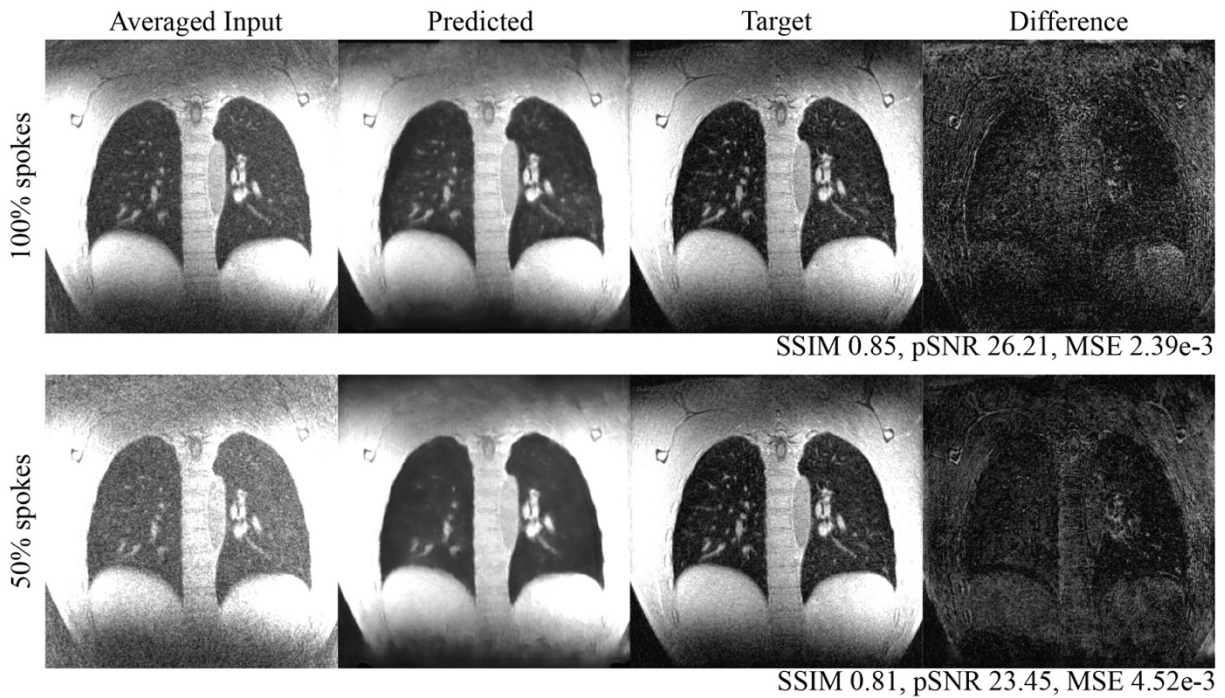
Figure 6.2 Example test set results with inputs generated using 100% and 50% of the raw data.

In both cases, there is a clear apparent SNR improvement. The sharpness of the diaphragm is a good marker of motion compensation, and is particularly sharp when using 100% of the raw data.

| Averaged Input | Predicted | Target | Difference |

100% spokes

SSIM 0.94, pSNR 33.42, MSE 4.55e-4

50% spokes

SSIM 0.90, pSNR 27.36, MSE 1.84e-3
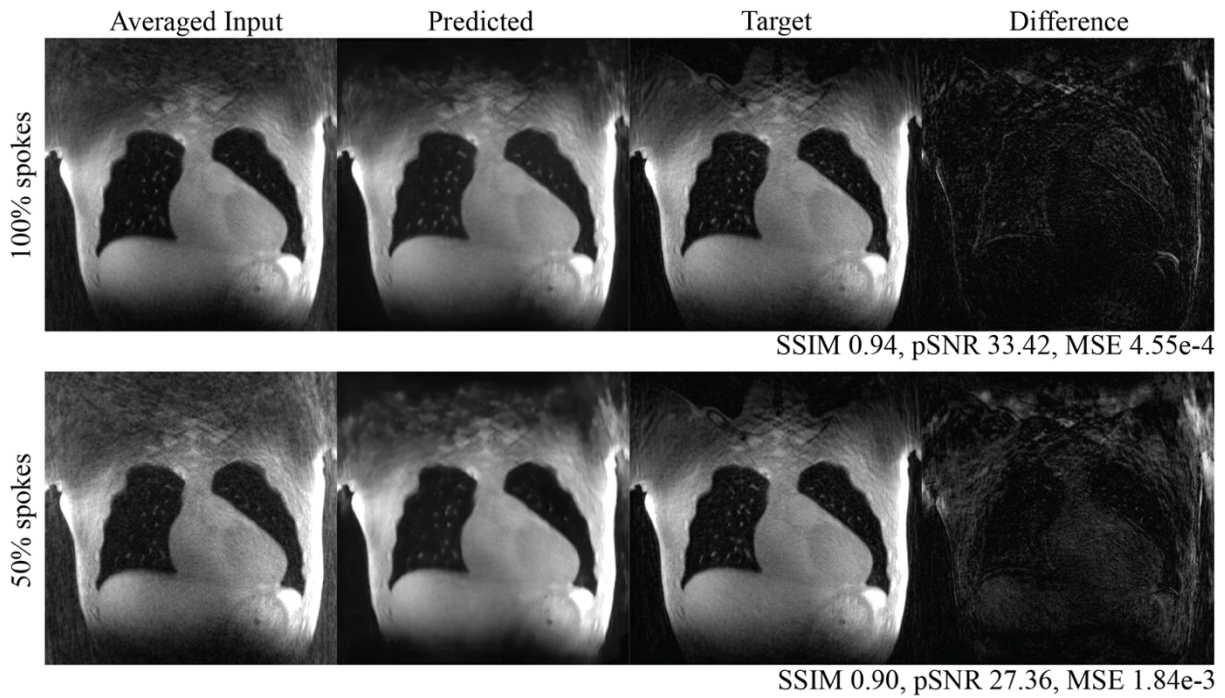
Figure 6.3 Another example test set results with inputs generated using 100% and 50% of the raw data.

69

The box plots of the structural similarity (SSIM), peak signal-to-noise ratio (pSNR), and mean squared error (MSE) metrics are shown in Figure 6.4. The mean structural similarity is 0.88±0.10 for 100% of spokes and 0.84±0.10 for 50% of spokes. The pSNR are 30.60±4.72 and 27.50±4.26, respectively, and the MSEs are 1.81e-3±3.07e-3 and 2.99e-3±3.60e-3.
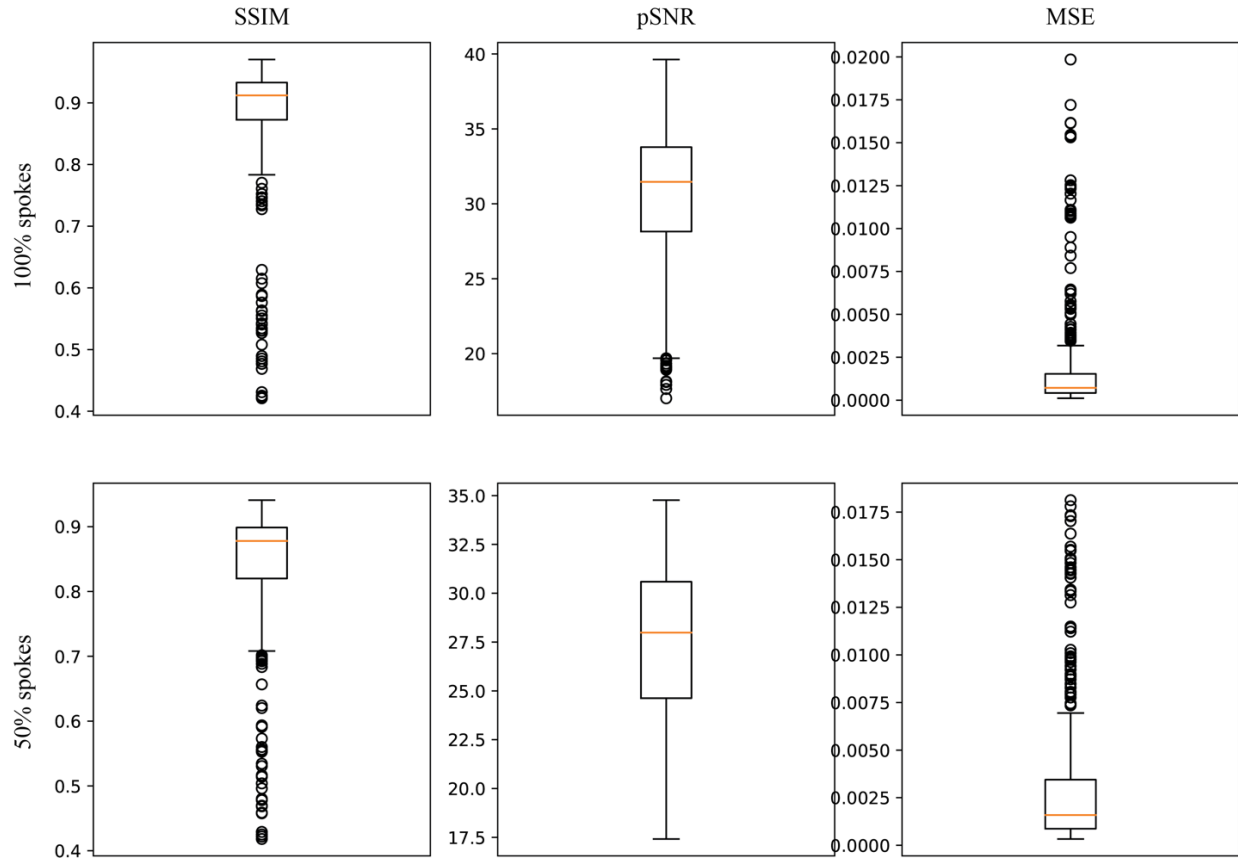
Figure 6.4 Structural similarity, peak signal-to-noise ratio, and mean squared error for 100% and 50% spoke motion-resolved NuFFT as network inputs.
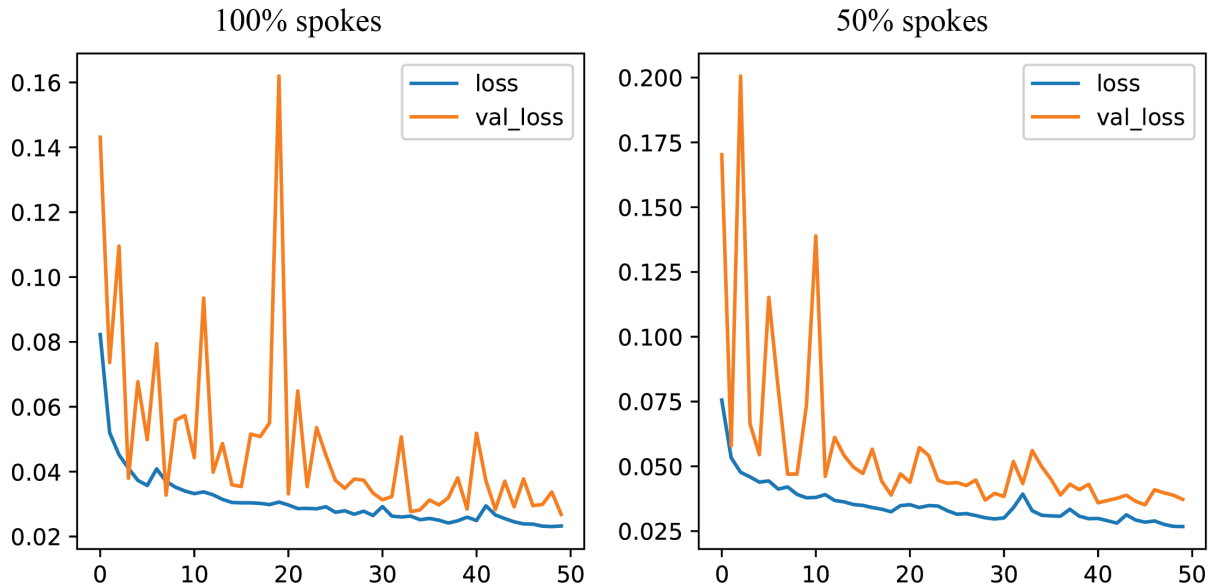
Figure 6.5 Network loss functions showing clear convergence.

6.4   Discussion

In this abstract, we used iMoCo reconstruction as target images, but it can be easily transferred to other motion-compensated reconstruction approaches and other organs that require motion compensation during image reconstruction, such as the heart and liver.

While the primary purpose of this approach is to accelerate the reconstruction time for motion-compensated reconstructions for 3D data, results from 50% spokes suggest that neural network-based motion compensation can also facilitate shortened scan times. This improvement would benefit pediatric patients who fail to stay still for a 5 min scan or adult patients who experience involuntary motion.

6.5 Conclusion

This abstract demonstrated the feasibility of using a convolutional neural network for motion-compensated proton lung MRI reconstruction and motion artifact removal. It accelerates the reconstruction for 3D radial UTE data substantially, shortening the required time from hours to minutes. Furthermore, it also shows potential to shorten the scan time, thus facilitating the clinical application of proton pulmonary UTE MRI.

Chapter 7 Quality Assessment of Ultrashort Echo Time (UTE) Proton Lung MRI in Pediatric Patients

7.1   Introduction

MRI is not routinely used in clinical practice for lung imaging because of the low proton density and respiratory motion artifact [43]. However, the ultrashort echo time (UTE) MRI technique can increase the signal in the lung. Recent developments in image reconstruction, such as iterative motion compensated (iMoCo) reconstruction [19], have improved respiratory motion management for free-breathing lung MRI scans. With the advantage of no ionizing radiation, MRI can benefit patients with immunodeficiency who often require repeat imaging, patients with heightened radiation sensitivity, and/or pediatric patients. In this abstract, we aim to evaluate the imaging quality of UTE lung MRI in the pediatric population.

7.2   Methods

All procedures are approved by the UCSF Institutional Review Board (IRB). In this pilot study, we included twelve pediatric patients (age 0-16, mean age 9.2, standard deviation 4.7 years old, 6 females, 6 males). Each patient went through a 5-minute free-breathing radial UTE MRI sequence, and the images were reconstructed using the iMoCo reconstruction. Two types of MR sequences were included: a 3D golden angle radial and a sequential stack of stars sequence. Six of the patients had CT within one year and formed the CT dataset in our study. Two experienced pediatric radiologists (M.A.Z. and R.D.) scored the quality of 16 structures in the chest using a Likert scale imaging quality scoring system [95]. The scoring criteria were 1 structure not seen, 2

structure blurred, 3 portion of structure blurred, 4 sharp borders of entire structure, and 5 sharp

borders with high subjective SNR.


```
┌─────────────────────────────────────────────────┐
│ 20 Pediatric Patients (age ≤ 18) with UTE lung MRI│
│      acquired between April 2018 to May 2021      │
└─────────────────────────────────────────────────┘
                         ↓
┌─────────────────────────────────────────────────┐
│ 13 MRI studies were available on PACS at the time of│
│    scoring and were scored by 2 experienced pediatric│
│                    radiologists                    │
└─────────────────────────────────────────────────┘
                         ↓
┌─────────────────────────────────────────────────┐
│     6 with CT within 1 year of MRI and were scored│
└─────────────────────────────────────────────────┘
                         ↓
┌─────────────────────────────────────────────────┐
│                Statistical Analysis                │
└─────────────────────────────────────────────────┘
```
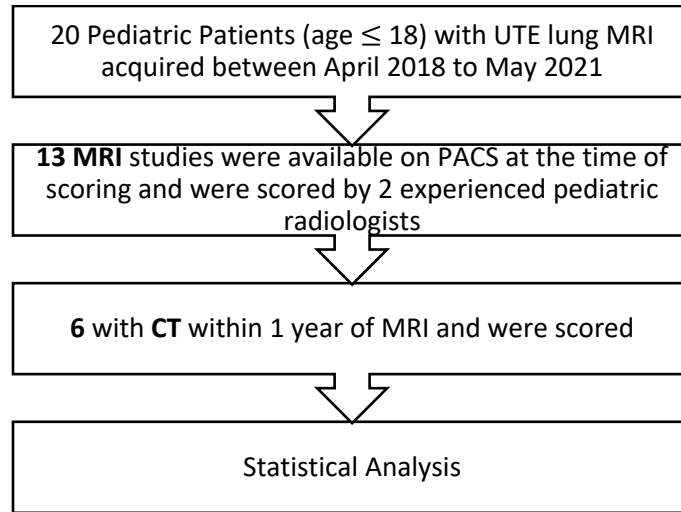
Figure 7.1 Flowchart of patient inclusion.

Table 7.1 Score table

Score	Structure Delineation Scoring Criteria
1	Structure not seen
2	Structure blurred/obscured
3	Portion of structure blurred/obscured
4	Sharp borders of entire structure
5	Sharp borders with high subjective SNR

7.3   Results

Statistical analysis shows an inter-class correlation (ICC) of 0.70, 0.73, and 0.72 for MR, CT,

and all scores, respectively, suggesting a moderate inter-reader correlation. Cohen's Kappa is

0.35, 0.35, and 0.37, respectively, suggesting fair inter-reader agreement. While CT has an overall higher score than MRI (p-value ≤ 0.00005), MR and CT scores are comparable in the aorta (ascending, descending and arch, average score MR 2.5, CT 2.4), central lung (MR 3.0, CT 3.2), and lobar bronchi (MR 3.3, CT 3.7), with a p-value > 0.05. In pulmonary arteries, pleura, peripheral lung, segmental, sub-segmental bronchi, bone, and chest wall soft tissue, CT outperforms MR with p-values ≤ 0.05. We also tested the influence of subgroups. Age under or greater than 12 is not a significant factor for the MRI score, nor is the 3D radial or stack of stars MRI sequence.
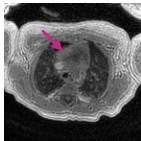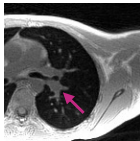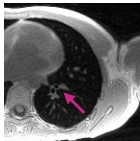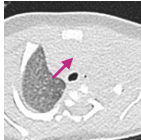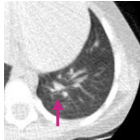
	1	2	3	4	5
MR	Ascending Aorta	Lobar Pulmonary Arteries	Segmental Bronchi	Aortic Arch	None
CT	Artery	Lobar Pulmonary Arteries	Subsegmental Bronchi	Pleura	None

Figure 7.2 Example Image of Scores.

UTE   CT

Pulmonary Nodules (5 yo)

UTE   CT

Ground Glass in chILD (4 yo)

UTE   CT

Bronchiolitis Obliterans (11 yo)

UTE   CT

Pneumatoceles (8 yo)
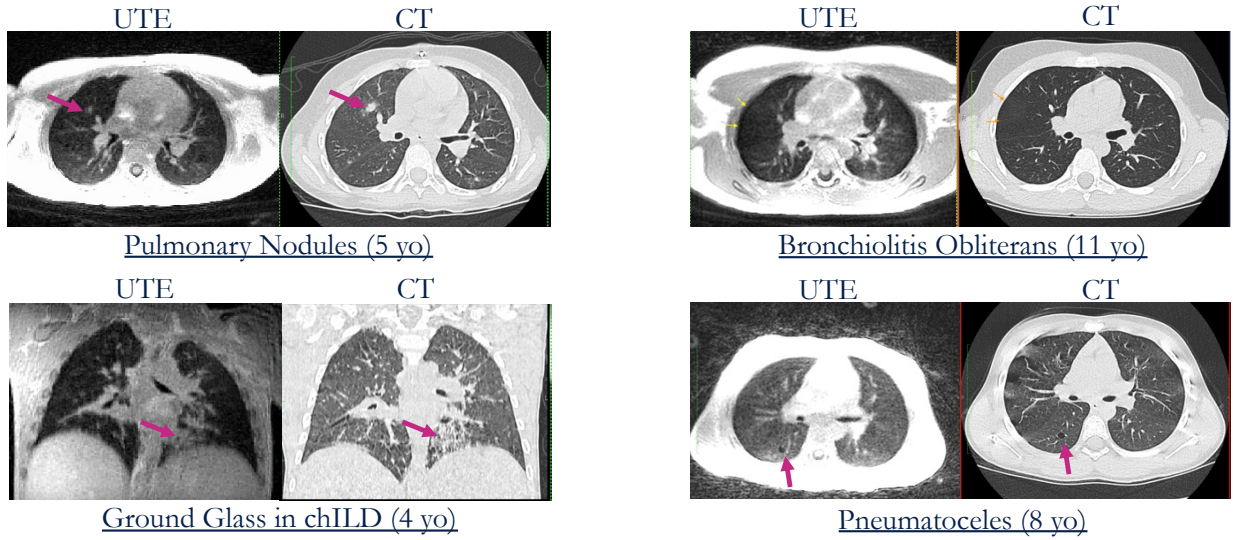
Figure 7.3 Example Lung Pathologies Observed with UTE MRI.

ns: p > 0.05
*: 0.01 < p ≤ 0.05
**: 0.001 < p ≤ 0.01
***: 0.0001 < p ≤ 0.001
****: p ≤ 0.0001
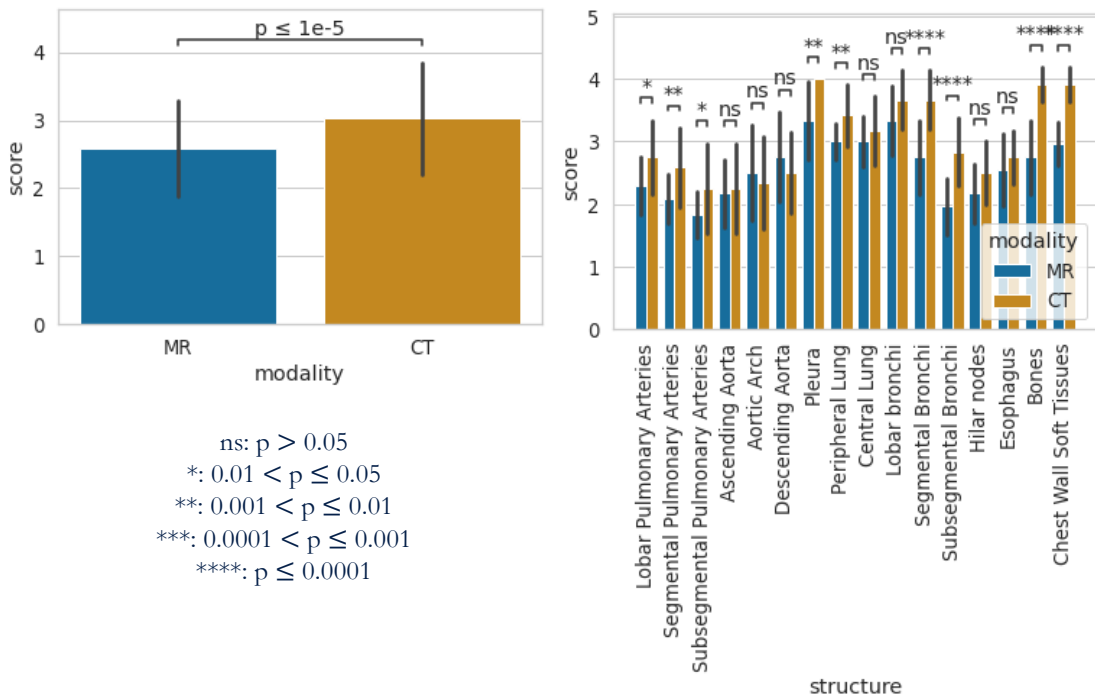
Figure 7.4 Bar plots of MR and CT scores.

CT has an overall higher score than MRI (p-value ≤ 0.00005). MR and CT scores are comparable in the aorta, central lung, and lobar bronchi, with a p-value > 0.05. In pulmonary arteries, pleura, peripheral lung, segmental, sub-segmental bronchi, bone, and chest wall soft tissue, CT outperforms MR with p-values ≤ 0.05.

76
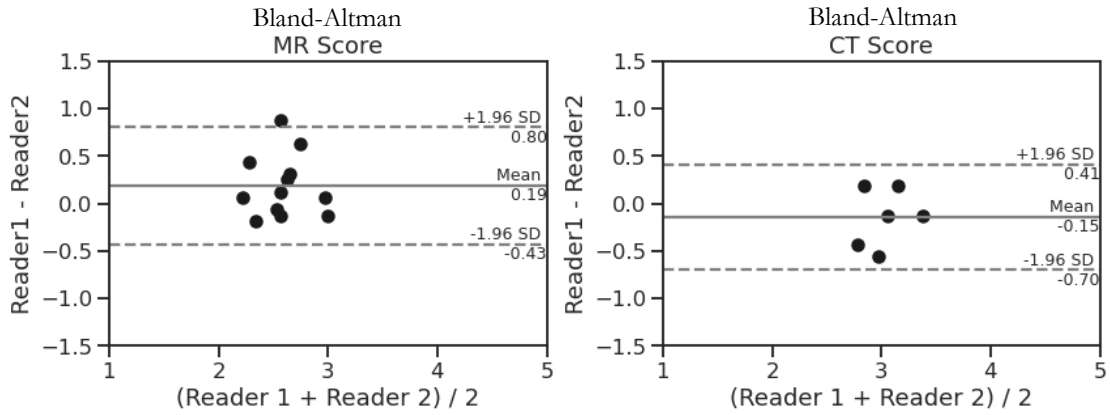
Figure 7.5 Bland-Altman plot shows a small bias and standard deviation.

7.4 Conclusion

While UTE MRI is inferior to CT when resolving smaller structures, it is comparable to its counterpart in some tissues such as the aorta, central lung, and lobar bronchi. UTE lung MRI can be useful for pediatric subjects who need long-term pulmonary monitoring or patients with immunodeficiency, or other patients with increased radiation sensitivity.

Chapter 8 Structural and Functional Proton UTE Lung MRI in Pediatric Pectus Deformity Patients

8.1 Introduction

Pectus deformity affects patients of different ages and about 1% of the population [96,97]. Pectus excavatum (or sunken chest) is the most common among them. The current clinical standard of care includes Haller Index [98] measurement on axial computed tomography (CT), pulmonary function test (PFT), and, if needed, Nuss surgical procedure [99]. However, CT has ionizing radiation, and PFT only provides global ventilation information. Recent advancement in lung MRI enables simultaneous structural and functional imaging from a single scan session. In this case study, we report the proton 3D UTE lung MRI results for three pediatric patients with pectus deformity. The structure images were used for Haller index measurements, and functional maps were used for regional function visualization to assist surgery decisions. To our knowledge, this is the first time that 3D UTE lung MRI ventilation has been reported in a specific patient population.

8.2 Methods

All procedures were approved by the University of California, San Francisco Institutional Review Board (IRB). Three pediatric patients with pectus excavatum or pectus carinatum (ages 13-17, 1 Female) were included in this case study. Written consent was obtained from both the patients and guardians. Each patient went through a 5-minute free-breathing proton ultrashort echo time (UTE) MRI of the lung [26] in a 3T scanner (GE Healthcare, Milwaukee, WI) using an

8-channel cardiac coil. The key scan parameters were FOV=32cm, resolution=1mm isotropic, # spokes=100,000. The iterative motion compensation (iMoCo) [19] technique was adopted for structural image reconstruction for the Haller Index measurement. The same raw data were binned into ten respiratory states, and each state was registered to the end-expiration state. The local volume change between the end-inspiration state and the end-expiration state indicates the regional air input during tidal breathing and thus forms the ventilation maps.

8.3 Results

The structural image of a patient with pectus excavatum (Figure 8.1 a) was used for Haller Index measurement in the PACS system. The Haller Index for this patient was calculated as 270mm/82.5mm=3.27. Figure 8.1 b shows the function map of the same patient in all three orthogonal views. The value represents the expansion percentage; for example, 0.3 means 30% volume was filled with air during tidal inhalation. The ventilation maps show that pectus excavatum affects the patient's ventilation function, especially in the area close to the anterior chest wall. In contrast, the patient with pectus carinatum has a lung function that's comparable to healthy volunteers (Figure 8.1 c).

8.4 Conclusion

In conclusion, the proton UTE MR structural images could be used in place of CT for Haller Index measurement. The ventilation maps anecdotally reflect the regional lung function and may assist the doctor's surgery decision for patients with pectus deformities. As for future directions, comparing ventilation maps before and after surgery can help validate functional measurements.

a) Structural MRI with measurements
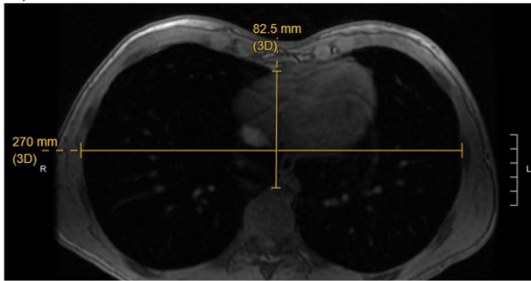
b) Functional ventilation maps of patient w/ pectus excavatum
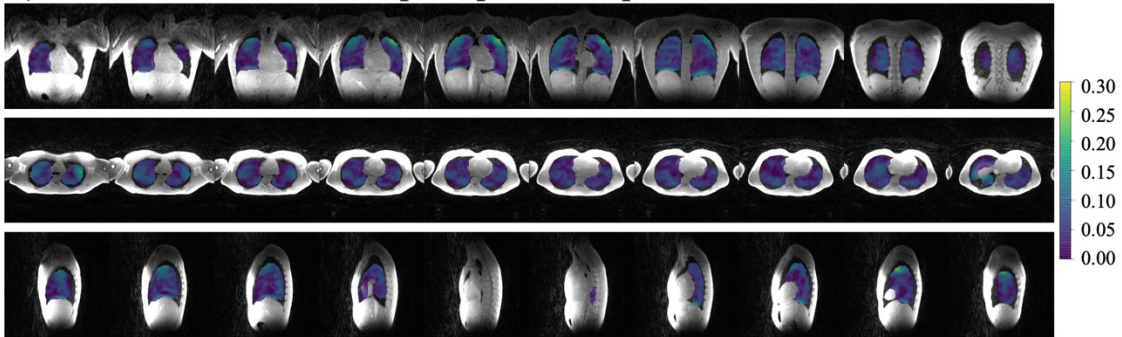
c) Functional ventilation maps of patient w/ pectus carinatum
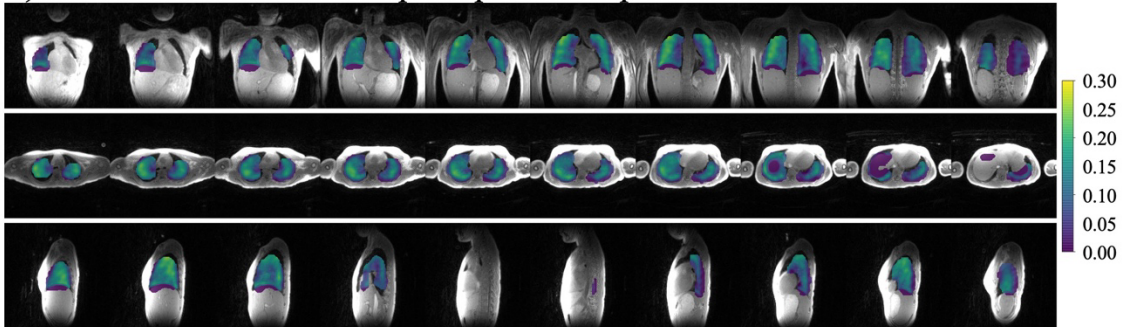
Figure 8.1 Example structural images and functional ventilation maps of patients.

Chapter 9 Summary and Future Work

9.1 Summary

In summary, this dissertation covers technical advancements and clinical applications of the UTE proton lung MRI.

In the reproducibility study, we tested four combinations of registration and calculation methods to quantify ventilation on 3D phase-resolved 1H UTE MRI of healthy volunteers. We conclude that cyclic registration is superior to SyN for ventilation purposes but more computationally expensive. Regional ventilation correlates better with segmentation lung volume, while specific ventilation is more reproducible.

We improved the motion-compensated low-rank (MoCoLoR) regularized reconstruction approach for simultaneous structural and functional lung MRI. This approach includes motion fields to reduce the rank and better share data across motion states during iterative reconstruction, efficiently using the data and resulting in high SNR in respiratory-resolved reconstructions. With data from a 5-minute scan, the MoCoLoR reconstructions can provide 1 mm isotropic high-resolution respiratory-resolved structural images, which were used to compute ventilation maps at the same high resolution.

We further validated the UTE 1H ventilation against 129Xe ventilation and pulmonary function testing. The 3D UTE 1H ventilation calculated from motion-compensated low-rank constrained reconstruction (MoCoLoR) has a positively correlated ventilation defect percentage (VDP)

compared with the gold standard 129Xe and a high spatial VDP accuracy. UTE 1H VDP also strongly correlated with global lung function measurements, including FEV1, FVC, and LCI.

The machine learning-based artifact removal project demonstrated the feasibility of using a convolutional neural network for motion-compensated proton lung MRI reconstruction. It accelerates the reconstruction of 3D radial UTE data substantially and potentially shortens the scan time.

The UTE 1H reader study suggests that while UTE MRI is inferior to CT when resolving smaller structures, it is comparable to its counterpart in some tissues, such as the aorta, central lung, and lobar bronchi. UTE lung MRI can be useful for pediatric subjects needing long-term pulmonary monitoring, patients with immunodeficiency, or other patients with increased radiation sensitivity.

Lastly, the clinical application of UTE 1H lung MRI to pediatric pectus deformity patients demonstrates that the proton UTE MR structural images could be used instead of CT for Haller Index measurement. The ventilation maps can reflect the regional lung function and may assist the doctor's surgery decision for patients with pectus deformities.

9.2   Future Work

9.2.1   Low-Field MRI

Proton lung MRI can benefit pediatric patients because it has no ionizing radiation, requires no additional equipment, and provides lung function information. However, the high susceptibility

due to the porous structure in conventional 3T led to fast T2* decay and low signal T2* = 0.74ms at 3T [100]. In low fields, T2* of the lung significantly increases to T2* = 10ms at 0.55T [101], resulting in a ten times larger acquisition window.

Previous works, such as T2 weighted lung imaging in 0.55T using Turbo Spin Echo acquisition [102] and spiral UTE pulmonary MRI at 0.55T system [93], demonstrated the feasibility of high-quality pulmonary imaging at low field. Based on our previous motion management and functional analysis techniques, we propose three potential innovations on lung MRI at 0.55T. First, apply radial UTE sequences for pulmonary MRI on a low-field system and provide structural and functional images for pediatric patients. Second, explore the feasibility of the T2-weighted Turbo Spin Echo. Due to the lengthened T2/T2* at 0.55T, high-quality T2w lung imaging is possible. Third, investigate the application of bSSFP sequence on low-field systems. bSSFP is highly desirable due to high SNR efficiency but typically suffers over the lung due to banding artifacts. These artifacts are no longer a major concern at 0.55T due to the reduced B0 inhomogeneity, enabling this powerful pulse sequence for lung MRI.

References

1. Wild, J. M. *et al.* MRI of the lung (1/3): Methods. *Insights into Imaging* **3**, 345–353 (2012).

2. Higano, N. S. *et al.* Retrospective respiratory self-gating and removal of bulk motion in pulmonary UTE MRI of neonates and adults. *Magnetic Resonance in Medicine* **77**, 1284–1295 (2017).

3. Feng, L. *et al.* XD-GRASP: Golden-angle radial MRI with reconstruction of extra motion-state dimensions using compressed sensing. *Magnetic Resonance in Medicine* **75**, 775–788 (2016).

4. Jiang, W. *et al.* Motion robust high resolution 3D free-breathing pulmonary MRI using dynamic 3D image self-navigator: Motion Robust High-Resolution 3D Pulmonary MRI. *Magn. Reson. Med* **79**, 2954–2967 (2018).

5. Tan, F., Zhu, X. & Larson, P. Motion-Compensated Low-Rank Reconstruction with Iterative Registration for Ventilation Analysis on Ultrashort Echo Time (UTE) Lung MRI. in (2022).

6. Zhu, X., Ong, F., Lustig, M. & Larson, P. Motion Compensated Low-Rank(MoCoLoR) constrained reconstruction with application to motion resolved lung MRI. in (2020).

7. Miller, G. W. *et al.* Advances in functional and structural imaging of the human lung using proton MRI. *NMR in Biomedicine* vol. 27 1542–1556 Preprint at https://doi.org/10.1002/nbm.3156 (2014).

8. Theilmann, R. J. *et al.* Quantitative MRI Measurement of Lung Density Must Account for the Change in T * 2 With Lung Inflation. **534**, 527–534 (2009).

9. Wild, J. M. *et al.* MRI of the lung (1/3): Methods. *Insights into Imaging* **3**, 345–353 (2012).

10. Bergin, C. J., Pauly, J. M. & Macovski, A. Lung parenchyma: Projection reconstruction MR imaging. *Radiology* **179**, 777–781 (1991).

11. Crapo, R. O. Pulmonary-function testing. *New England Journal of Medicine* **331**, 25–30 (1994).

12. Woods, J. C. *et al.* Current state of the art MRI for the longitudinal assessment of cystic fibrosis. *Journal of Magnetic Resonance Imaging* (2019) doi:10.1002/jmri.27030.

13. Zucker, E. J., Cheng, J. Y., Haldipur, A., Carl, M. & Vasanawala, S. S. Free-breathing pediatric chest MRI: Performance of self-navigated golden-angle ordered conical ultrashort echo time acquisition. *Journal of Magnetic Resonance Imaging* **47**, 200–209 (2018).

14. Salerno, M. *et al.* Hyperpolarized noble gas MR imaging of the lung: Potential clinical applications. *European Journal of Radiology* **40**, 33–44 (2001).

15. Bauman, G. *et al.* Non-contrast-enhanced perfusion and ventilation assessment of the human lung by means of Fourier decomposition in proton MRI. *Magnetic Resonance in Medicine* **62**, 656–664 (2009).

16. Voskrebenzev, A. *et al.* Feasibility of quantitative regional ventilation and perfusion mapping with phase-resolved functional lung (PREFUL) MRI in healthy volunteers and COPD, CTEPH, and CF patients. *Magnetic Resonance in Medicine* **79**, 2306–2314 (2018).

17. Moher Alsady, T. *et al.* MRI-derived regional flow-volume loop parameters detect early-stage chronic lung allograft dysfunction. *Journal of Magnetic Resonance Imaging* **50**, 1873–1882 (2019).

18. Feng, L. *et al.* XD-GRASP: Golden-angle radial MRI with reconstruction of extra motion-state dimensions using compressed sensing. *Magn. Reson. Med.* **75**, 775–788 (2016).

19. Zhu, X., Chan, M., Lustig, M., Johnson, K. M. & Larson, P. E. Z. Iterative motion-compensation reconstruction ultra-short TE (iMoCo UTE) for high-resolution free-breathing pulmonary MRI. *Magn Reson Med* **83**, 1208–1221 (2020).

20. Ding, Z. *et al.* Dynamic pulmonary MRI using motion-state weighted motion-compensation (MOSTMOCO) reconstruction with ultrashort TE : A structural and functional study. *Magnetic Resonance in Med* **88**, 224–238 (2022).

21. Nishimura, D. G. *Principles of Magnetic Resonance Imaging*. (Lulu.com, 2010).

22. Coyne, K. MRI: A Guided Tour - Magnet Academy. https://nationalmaglab.org/magnet-academy/read-science-stories/science-simplified/mri-a-guided-tour/.

23. Carter, J. W. MRI: The Basics, 3rd ed. *American Journal of Roentgenology* **197**, W361–W361 (2011).

24. Robson, M. D., Gatehouse, P. D., Bydder, M. & Bydder, G. M. Magnetic Resonance: An Introduction to Ultrashort TE (UTE) Imaging. *Journal of Computer Assisted Tomography* **27**, 825–846 (2003).

25. Tyler, D. J., Robson, M. D., Henkelman, R. M., Young, I. R. & Bydder, G. M. Magnetic resonance imaging with ultrashort TE (UTE) PULSE sequences: Technical considerations. *J. Magn. Reson. Imaging* **25**, 279–289 (2007).

26. Johnson, K. M., Fain, S. B., Schiebler, M. L. & Nagle, S. Optimized 3D ultrashort echo time pulmonary MRI: Optimized 3D Ultrashort Echo Time Pulmonary MRI. *Magn. Reson. Med.* **70**, 1241–1250 (2013).

27. Feng, L. GOLDEN-ANGLE Radial MRI: Basics, Advances, and Applications. *Magnetic Resonance Imaging* **56**, 45–62 (2022).

28. Biederer, J. *et al.* MRI of the lung (2/3). Why... when ... how? *Insights into Imaging* **3**, 355–371 (2012).

29. Bauman, G. *et al.* Non-contrast-enhanced perfusion and ventilation assessment of the human lung by means of Fourier decomposition in proton MRI. *Magnetic Resonance in Medicine* **62**, 656–664 (2009).

30. Boucneau, T., Fernandez, B., Larson, P., Darrasse, L. & Maître, X. 3D Magnetic Resonance Spirometry. *Scientific Reports* **10**, 1–12 (2020).

31. Johnson, K. M., Fain, S. B., Schiebler, M. L. & Nagle, S. Optimized 3D ultrashort echo time pulmonary MRI. *Magnetic Resonance in Medicine* **70**, 1241–1250 (2013).

32. Uecker, M., Tamir, J. & Lustig, M. BART Toolbox for Computational Magnetic Resonance Imaging. doi:DOI: 10.5281/zenodo.592960.

33. Metz, C. T., Klein, S., Schaap, M., van Walsum, T. & Niessen, W. J. Nonrigid registration of dynamic medical imaging data using nD+t B-splines and a groupwise optimization approach. *Medical Image Analysis* **15**, 238–249 (2011).

34. Avants, B. B., Epstein, C. L., Grossman, M. & Gee, J. C. Symmetric diffeomorphic image registration with cross-correlation: Evaluating automated labeling of elderly and neurodegenerative brain. *Medical Image Analysis* **12**, 26–41 (2008).

35. Klein, S., Staring, M., Murphy, K., Viergever, M. a. & Pluim, J. elastix: A Toolbox for Intensity-Based Medical Image Registration. *IEEE Transactions on Medical Imaging* **29**, 196–205 (2010).

36. Avants, B. B. *et al.* A reproducible evaluation of ANTs similarity metric performance in brain image registration. *NeuroImage* **54**, 2033–2044 (2011).

37. Tustison, N. J. *et al.* Convolutional Neural Networks with Template-Based Data Augmentation for Functional Lung Image Quantification. *Academic Radiology* **26**, 412–423 (2019).

38. Chassagnon, G. *et al.* Use of Elastic Registration in Pulmonary MRI for the Assessment of Pulmonary Fibrosis in Patients with Systemic Sclerosis. *Radiology* **291**, 487–492 (2019).

39. Castillo, R., Castillo, E., Martinez, J. & Guerrero, T. TU-B-204B-04: Ventilation from Four Dimensional Computed Tomography: Density versus Jacobian Methods. *Medical Physics* **37**, 3377 (2010).

40. Klimeš, F. *et al.* 3D phase-resolved functional lung ventilation MR imaging in healthy volunteers and patients with chronic pulmonary disease. *Magnetic Resonance in Medicine* **85**, 912–925 (2021).

41. Zapke, M. *et al.* Magnetic resonance lung function - A breakthrough for lung imaging and functional assessment? A phantom study and clinical trial. *Respiratory Research* **7**, 1–9 (2006).

42. Sá, R. C. *et al.* Vertical distribution of specific ventilation in normal supine humans measured by oxygen-enhanced proton MRI. *Journal of Applied Physiology* **109**, 1950–1959 (2010).

43. Wild, J. M. *et al.* MRI of the lung (1/3): methods. *Insights Imaging* **3**, 345–353 (2012).

44. Chappell, K. E. *et al.* Magnetic resonance imaging of the liver with ultrashort TE (UTE) pulse sequences. *J. Magn. Reson. Imaging* **18**, 709–713 (2003).

45. Torres, L. *et al.* "Structure-Function Imaging of Lung Disease Using Ultrashort Echo Time MRI". *Academic Radiology* **26**, 431–441 (2019).

46. Biederer, J. *et al.* Lung Morphology: Fast MR Imaging Assessment with a Volumetric Interpolated Breath-Hold Technique: Initial Experience with Patients. *Radiology* **226**, 242–249 (2003).

47. Ehman, R., McNamara, M., Pallack, M., Hricak, H. & Higgins, C. Magnetic resonance imaging with respiratory gating: techniques and advantages. *American Journal of Roentgenology* **143**, 1175–1182 (1984).

48. Koch, N. *et al.* Evaluation of internal lung motion for respiratory-gated radiotherapy using MRI: Part I—correlating internal lung motion with skin fiducial motion. *International Journal of Radiation Oncology*Biology*Physics* **60**, 1459–1472 (2004).

49. McClelland, J. R., Hawkes, D. J., Schaeffter, T. & King, A. P. Respiratory motion models: A review. *Medical Image Analysis* **17**, 19–42 (2013).

50. Shattuck, M. D. *et al.* MR microimaging of the lung using volume projection encoding. *Magnetic Resonance in Medicine* **38**, 938–942 (1997).

51. Zucker, E. J., Cheng, J. Y., Haldipur, A., Carl, M. & Vasanawala, S. S. Free-breathing pediatric chest MRI: Performance of self-navigated golden-angle ordered conical ultrashort echo time acquisition. *Journal of Magnetic Resonance Imaging* **47**, 200–209 (2018).

52. Morokoff, W. J. & Caflisch, R. E. Quasi-Random Sequences and Their Discrepancies. *SIAM Journal on Scientific Computing* **15**, 1251–1279 (1994).

53. Wong, S. T. S. & Roos, M. S. A strategy for sampling on a sphere applied to 3D selective RF pulse design. *Magnetic Resonance in Medicine* vol. 32 778–784 Preprint at https://doi.org/10.1002/mrm.1910320614 (1994).

54. Chan, R. W., Ramsay, E. A., Cunningham, C. H. & Plewes, D. B. Temporal stability of adaptive 3D radial MRI using multidimensional golden means. *Magnetic Resonance in Medicine* **61**, 354–363 (2009).

55. Asif, M. S., Hamilton, L., Brummer, M. & Romberg, J. Motion-adaptive spatio-temporal regularization for accelerated dynamic MRI. *Magnetic Resonance in Medicine* **70**, 800–812 (2013).

56. Bonanno, G. *et al.* Self-navigation with compressed sensing for 2D translational motion correction in free-breathing coronary MRI: A feasibility study. *PLoS ONE* **9**, (2014).

57. Cheng, J. Y. *et al.* Free-breathing pediatric MRI with nonrigid motion correction and acceleration. *Journal of Magnetic Resonance Imaging* **42**, 407–420 (2015).

58. Küstner, T. *et al.* Self-navigated 4D cartesian imaging of periodic motion in the body trunk using partial k-space compressed sensing. *Magnetic Resonance in Medicine* **78**, 632–644 (2017).

59. Usman, M. *et al.* Motion corrected compressed sensing for free-breathing dynamic cardiac MRI. *Magnetic Resonance in Medicine* **70**, 504–516 (2013).

60. Batchelor, P. G. *et al.* Matrix description of general motion correction applied to multishot images. *Magn. Reson. Med.* **54**, 1273–1280 (2005).

61. Furnival, T., Leary, R. K. & Midgley, P. A. Denoising time-resolved microscopy image sequences with singular value thresholding. *Ultramicroscopy* **178**, 112–124 (2017).

62. Nakarmi, U., Wang, Y., Lyu, J., Liang, D. & Ying, L. A Kernel-Based Low-Rank (KLR) Model for Low-Dimensional Manifold Recovery in Highly Accelerated Dynamic MRI. *IEEE Transactions on Medical Imaging* **36**, 2297–2307 (2017).

63. Ong, F. & Lustig, M. Beyond Low Rank + Sparse: Multiscale Low Rank Matrix Decomposition. *IEEE Journal on Selected Topics in Signal Processing* **10**, 672–687 (2016).

64. Otazo, R., Candès, E. & Sodickson, D. K. Low-rank plus sparse matrix decomposition for accelerated dynamic MRI with separation of background and dynamic components. *Magnetic Resonance in Medicine* **73**, 1125–1136 (2015).

65. Yoon, H., Kim, K. S., Kim, D., Bresler, Y. & Ye, J. C. Motion adaptive patch-based low-rank approach for compressed sensing cardiac cine MRI. *IEEE Transactions on Medical Imaging* **33**, 2069–2085 (2014).

66. Chen, X., Salerno, M., Yang, Y. & Epstein, F. H. Motion-compensated compressed sensing for dynamic contrast-enhanced MRI using regional spatiotemporal sparsity and region tracking: Block low-rank sparsity with motion-guidance (BLOSM). *Magnetic Resonance in Medicine* **72**, 1028–1038 (2014).

67. Cruz, G. *et al.* LOW-RANK motion correction for accelerated free-breathing first-pass myocardial perfusion imaging. *Magnetic Resonance in Med* mrm.29626 (2023) doi:10.1002/mrm.29626.

68. Phair, A., Cruz, G., Qi, H., Botnar, R. M. & Prieto, C. Free-running 3D whole-heart T_1 and T_2 mapping and cine MRI using low-rank reconstruction with non-rigid cardiac motion correction. *Magnetic Resonance in Med* **89**, 217–232 (2023).

69. Bauman, G. *et al.* Non-contrast-enhanced perfusion and ventilation assessment of the human lung by means of fourier decomposition in proton MRI: Non-CE Functional Lung Imaging in ^{1}H MRI. *Magn. Reson. Med.* **62**, 656–664 (2009).

70. Voskrebenzev, A. *et al.* Feasibility of quantitative regional ventilation and perfusion mapping with phase-resolved functional lung (PREFUL) MRI in healthy volunteers and COPD, CTEPH, and CF patients. *Magn. Reson. Med* **79**, 2306–2314 (2018).

71. Klimeš, F. *et al.* 3D phase-resolved functional lung ventilation MR imaging in healthy volunteers and patients with chronic pulmonary disease. *Magn. Reson. Med.* **85**, 912–925 (2021).

72. Boucneau, T., Fernandez, B., Larson, P., Darrasse, L. & Maître, X. 3D Magnetic Resonance Spirometry. *Sci Rep* **10**, 9649 (2020).

73. Zapke, M. *et al.* Magnetic resonance lung function – a breakthrough for lung imaging and functional assessment? A phantom study and clinical trial. *Respir Res* **7**, 106 (2006).

74. Winkler, S. A. *et al.* Evaluation of a Flexible 12-Channel Screen-printed Pediatric MRI Coil. *Radiology* **291**, 180–185 (2019).

75. Frank Ong, Jonathan Martin, Will Grissom, Siddharth Srinivasan, Kevin M. Johnson, Chris Huynh, Arjun Desai, Zhitao-Li, Jon Tamir, Chris Sandino, EfratShimron, David Zeng, Nikolai Mickevicius. (2022) mikgroup/sigpy: Minor release to trigger Zenodo for DOI. doi: 10.5281/zenodo.5893788.

76. Sá, R. C. *et al.* Vertical distribution of specific ventilation in normal supine humans measured by oxygen-enhanced proton MRI. *Journal of Applied Physiology* **109**, 1950–1959 (2010).

77. Tustison, N. J. *et al.* Convolutional Neural Networks with Template-Based Data Augmentation for Functional Lung Image Quantification. *Academic Radiology* **26**, 412–423 (2019).

78. Santyr, G. *et al.* Hyperpolarized Gas Magnetic Resonance Imaging of Pediatric Cystic Fibrosis Lung Disease. *Academic Radiology* **26**, 344–354 (2019).

79. Veldhoen, S. *et al.* Self-gated Non–Contrast-enhanced Functional Lung MR Imaging for Quantitative Ventilation Assessment in Patients with Cystic Fibrosis. *Radiology* **283**, 242–251 (2017).

80. Mugler, J. P. & Altes, T. A. Hyperpolarized ^{129}Xe MRI of the human lung. *J. Magn. Reson. Imaging* **37**, 313–331 (2013).

81. Kirby, M. Hyperpolarized 3He Magnetic Resonance Functional Imaging Semiautomated Segmentation. *Academic Radiology* **19**, 12 (2012).

82. He, M. *et al.* Extending Semiautomatic Ventilation Defect Analysis for Hyperpolarized 129Xe Ventilation MRI. *Academic Radiology* **21**, 1530–1541 (2014).

83. Fischer, A. *et al.* SElf-gated Non-Contrast-Enhanced FUnctional Lung imaging (SENCEFUL) using a quasi-random fast low-angle shot (FLASH) sequence and proton MRI: SELF-GATED NON-CONTRAST-ENHANCED FUNCTIONAL LUNG IMAGING (SENCEFUL). *NMR Biomed.* **27**, 907–917 (2014).

84. Capaldi, D. P. I. *et al.* Free-breathing Pulmonary 1H and Hyperpolarized 3He MRI. *Academic Radiology* **22**, 320–329 (2015).

85. Couch, M. J. *et al.* Comparison of Functional Free-Breathing Pulmonary 1H and Hyperpolarized 129Xe Magnetic Resonance Imaging in Pediatric Cystic Fibrosis. *Academic Radiology* **28**, e209–e218 (2021).

86. Kaireit, T. F. *et al.* Flow Volume Loop and Regional Ventilation Assessment Using Phase-Resolved Functional Lung (PREFUL) MRI : Comparison With ^{129}XENON Ventilation MRI and Lung Function Testing. *J Magn Reson Imaging* **53**, 1092–1105 (2021).

87. Smith, L. J. *et al.* The assessment of short- and long-term changes in lung function in cystic fibrosis using ^{129} Xe MRI. *Eur Respir J* **56**, 2000441 (2020).

88. Johnson, K. M., Fain, S. B., Schiebler, M. L. & Nagle, S. Optimized 3D ultrashort echo time pulmonary MRI. *Magnetic Resonance in Medicine* **70**, 1241–1250 (2013).

89. Eddy, R. L. *et al.* Pulmonary MRI and Cluster Analysis Help Identify Novel Asthma Phenotypes. *Magnetic Resonance Imaging* **56**, 1475–1486 (2022).

90. Avants, B., Epstein, C., Grossman, M. & Gee, J. Symmetric diffeomorphic image registration with cross-correlation: Evaluating automated labeling of elderly and neurodegenerative brain. *Medical Image Analysis* **12**, 26–41 (2008).

91. Lytras, T. rspiro. (2020).

92. Quanjer, P. H. *et al.* Multi-ethnic reference values for spirometry for the 3–95-yr age range: the global lung function 2012 equations. *Eur Respir J* **40**, 1324–1343 (2012).

93. Javed, A. *et al.* Self-gated 3D stack-of-spirals UTE pulmonary imaging at 0.55T. *Magnetic Resonance in Med* **87**, 1784–1798 (2022).

94. Ronneberger, O., Fischer, P. & Brox, T. U-Net: Convolutional Networks for Biomedical Image Segmentation. Preprint at http://arxiv.org/abs/1505.04597 (2015).

95. Nagle, S. K. *et al.* Ultrashort echo time MRI of lung pathology in humans. *Proc. Intl. Soc. Mag. Reson. Med. 20 (2012)* 1.

96. Williams, A. M. & Crabbe, D. C. G. Pectus deformities of the anterior chest wall. *Paediatric Respiratory Reviews* **4**, 237–242 (2003).

97. Obermeyer, R. J., Cohen, N. S. & Jaroszewski, D. E. The physiologic impact of pectus excavatum repair. *Seminars in Pediatric Surgery* **27**, 127–132 (2018).

98. Haller, J. A., Kramer, S. S. & Lietman, S. A. Use of CT scans in selection of patients for pectusexcavatum surgery: A preliminary report. *Journal of Pediatric Surgery* **22**, 904–906 (1987).

99. Nuss, D. & Kelly, R. E. Minimally Invasive Surgical Correction of Chest Wall Deformities in Children (Nuss Procedure). *Advances in Pediatrics* **55**, 395–410 (2008).

100. Yu, J., Xue, Y. & Song, H. K. Comparison of lung T_2* during free-breathing at 1.5 T and 3.0 T with ultrashort echo time imaging: Lung T_2* Measurements at 1.5 T and 3.0 T with UTE. *Magn. Reson. Med.* **66**, 248–254 (2011).

101. Campbell-Washburn, A. E. *et al.* Opportunities in Interventional and Diagnostic Imaging by Using High-Performance Low-Field-Strength MRI. *Radiology* **293**, 384–393 (2019).

102. Campbell-Washburn, A. E. *et al.* T2-weighted Lung Imaging Using a 0.55-T MRI System. *Radiology: Cardiothoracic Imaging* **3**, e200611 (2021).

Publishing Agreement

It is the policy of the University to encourage open access and broad distribution of all theses, dissertations, and manuscripts. The Graduate Division will facilitate the distribution of UCSF theses, dissertations, and manuscripts to the UCSF Library for open access and distribution. UCSF will make such theses, dissertations, and manuscripts accessible to the public and will take reasonable steps to preserve these works in perpetuity.

I hereby grant the non-exclusive, perpetual right to The Regents of the University of California to reproduce, publicly display, distribute, preserve, and publish copies of my thesis, dissertation, or manuscript in any form or media, now existing or later derived, including access online for teaching, research, and public service purposes.

DocuSigned by:

_____   5/5/2023
F0AFB315E802480...   Author Signature   Date